Distributed Tie-Line Power Flow Control of Autonomous DC Microgrid Clusters

Shivraman Mudaliyar, *Student Member, IEEE*, Bhanu Duggal, and Sukumar Mishra, *Senior Member, IEEE*

***Abstract*—For microgrids (MGs) owned by different utilities, it is always desirable that the steady state impact of load or generation changes in one MG, does not affect the generation cost in another MG. To ensure this, the power flow through the tie-line is typically regulated at a pre-scheduled value thereby enforcing the individual MGs to manage their respective load at steady state. To this end, this article presents a distributed control scheme to regulate tie-line power flow between two autonomous dc MG clusters. In this article, a unifying hierarchical control scheme based on distributed communication is proposed where the tie-line power flow control based on a pinning control strategy is unified with the distributed optimization and average voltage regulation control loops. The distributed optimization utilizes economic dispatch to minimize the operating costs of the DG, while the average voltage control regulates the MGs average voltage at its nominal value. With the application of this approach, the responsibility of tie-line regulation is distributed in an economic manner without degrading the voltage quality in the system. Time-domain simulations, real-time simulation using Ethernet-based transmission control protocol/internet protocol (TCP/IP) communication, and experimental results are presented to validate the performance of proposed distributed control under normal and faulty system conditions.**

***Index Terms*—DC microgrid (MG) clusters, distributed control, hierarchical control, pinning control, power flow control, stability analysis, voltage control.**

I. Introduction

DC MICROGRIDS (MGs) are now gaining increased attention due to their several benefits over ac MGs. Conversion losses are reduced as majority of renewable energy sources (RES) like photovoltaics (PV) and alternative sources like fuel cells and energy storage systems (ESS) inherently provide a dc output. Moreover, control of dc MGs is much simpler than ac MGs since the need for frequency control and synchronization is eliminated [1]–[4].

Manuscript received October 12, 2019; revised January 23, 2020; accepted March 3, 2020. Date of publication March 15, 2020; date of current version June 23, 2020. This work was supported by Department of Science and Technology, Government of India, under Project Identification and Demonstration of Cost-effective Technologies to Maximize Habitat Energy self-sufficiency, File No: TMD/CERI/BEE/2016/096(G). Recommended for publication by Associate Editor Dr. Y. Tang. *(Corresponding author: Shivraman Mudaliyar.)*

Shivraman Mudaliyar and Sukumar Mishra are with the Department of Electrical Engineering, Indian Institute of Technology, New Delhi 110016, India (e-mail: shiv.raman2k7@gmail.com; sukumariitdelhi@gmail.com).

Bhanu Duggal is with the Department of Electrical and Electronic Engineering, Imperial College London, London SW7 2AZ, U.K. (e-mail: bhanu.duggal11@gmail.com).

Color versions of one or more of the figures in this article are available online at http://ieeexplore.ieee.org.

Digital Object Identifier 10.1109/TPEL.2020.2980882

The operation and control of a MG is typically implemented using a hierarchical control structure [5]. At the primary level, droop control loop provides voltage reference to inner control loops to achieve proportional power sharing among sources within the MG. However, to achieve power sharing in systems where line impedances are not negligible, higher value of droop gain is needed. But, a higher droop gain results in large voltage drifts which may be detrimental for overall system stability. The aforementioned problem of voltage regulation can be tackled by adopting adaptive droop control [6], [7]. Another possible way to compensate voltage drifts is to use a secondary controller. Several authors [8], [9] have proposed a secondary control approach to ensure proper load sharing and improved voltage regulation. Authors in [10] combined voltage regulator with an optimizer to reduce overall generation cost.

Tertiary control is at the highest level of control hierarchy and is responsible to manage the power flow to/from the MG to an external power network which can be grid or another MG [11]–[14]. A schedule for power exchange is decided between the system operators of the two networks based on which tertiary controller adjusts voltage set points for the MG and communicates to the secondary and primary controllers. Islanded MGs heavily reliant on RES are prone to severe disturbances arising due to drastic changes in load or generation [15]. Such a disturbance can over-stress other units which can result in system failure. Since it is not always feasible and economically viable to add storage or additional generation, a practical solution to this issue is to establish a dc MG cluster by interconnecting nearby MGs. Along with maximum utilization of resources dc MG cluster enables neighboring MGs to support each other (dynamically) during emergency conditions. However, it is to be noted that interconnection of MGs requires a suitable tertiary or secondary control strategy to manage power flow between them. Conventionally, centralized control systems are used to implement tertiary control [16] where high bandwidth communication links are set up between the centralized controller and agents. However, these systems are exposed to single point-of-failure which risks system stability and makes the system vulnerable to cascaded failures and eventual collapse [15]. Some works in the literature have considered distributed tertiary control as it offers autonomous management along with improved reliability, scalability, and a simpler communication network. Shaifee *et al.* [5] presented a distributed power flow control scheme to handle power sharing between interconnected MGs in a cluster. In this article, authors have proposed adaptive droop control to balance SOC of batteries in an MG and to use the average SOC of local

MGs to define the tie-line power reference. However, only common dc bus topology for MGs was considered and impedances for distribution lines within an MG were neglected. The authors in [17] have presented an optimization and distributed control strategy for interconnected autonomous ac MGs. The authors claim to employ distributed control strategy for tie-line power flow control. However, no information regarding the cyber network that implements the distributed control is presented. A decentralized control method for interconnected dc MG clusters connected to a common dc bus is presented in [18]. Each nanogrid cluster represents a community household equipped with PV-battery system. Spatial distribution of households is not considered in the above work, and hence, the proposed control strategy is restricted to be applied for a common dc bus architecture and may not be suitable for a multibus MG system interconnected by multiple tie-lines. A power-line signaling (PLS)-based distributed control is proposed for a common dc bus architecture-based low voltage dc microgrid (LVDC) MG in [19]. A distributed energy management strategy (DEMS)-based on PLS is proposed for coordinated and simultaneous management of multiple battery strings and renewable energy sources. Though, the authors have extended the application of DEMS to incorporate more number of renewable energy sources, it is unclear whether the proposed control strategy can yield similar results for control of multibus interconnected dc MG clusters. The authors in [20], have proposed an isolated interlinking bidirectional converters to connect multiple dc MG clusters. While the control of power flow among MGs is flexible with this approach, it demands an additional investment. Moreover, a common dc bus topology is considered and spatial distribution of resources and their heterogeneity have been neglected. A coordinated power control strategy for multiple ac and dc subgrids is presented in [21]. The coordinated strategy utilizes voltage- and frequency-based droop control to assist the subgrids (ac or dc) under dynamic conditions. This article is also based on a common dc bus topology and did not exercise any tie-line power flow strategy among the MGs. In [22], authors introduced a cooperative two level distributed tertiary control strategy where local controller balances all the source currents within an MG; global controller adjusts voltage set points based on loading mismatch in neighboring MGs. This article completely neglected the heterogeneity of energy sources and only considered a rectified ac source interfaced using a buck converter. Whereas, typical dc MGs are composed of various types of sources such as PV, diesel generator (DG), fuel cells, and microturbines along with ESS such as batteries and supercapacitors.

From the above discussions, it is evident that previous studies have developed strategies such as SOC equalization and balancing of source currents for tertiary control in a dc MG cluster. However, the results presented in the abovementioned works, may be suboptimal since these studies do not consider optimal resource management of the controllable sources. Another drawback in the above approaches is that they do not consider that MGs participating in a cluster may belong to different entities. Consequently, any load/generation changes in one MG should not affect the generation cost in the other MG. Therefore, this article focuses on achieving optimal generation among sources within a MG by using distributed economic dispatch approach. Moreover, a pinning-based distributed tie-line controller is proposed in order to regulate tie-line power as per mutually agreed power exchange schedule. Since the information of power deviation from its scheduled value is only available local to the boundary bus, the distributed pining control strategy can be applied, where a sparse communication network can be utilized to diffuse the real-time information exchange among the participating generators in the system. This way the responsibility of tie-line regulation exercised by the MG can be distributed in an economic manner without degrading the voltage quality in the system. A brief survey related to the distributed consensus of multiagent systems can be found in [23].

An important consideration in this article is that the tie-line schedule is selected such that the MG exporting power has sufficient reserve during the considered time interval (can be 15 min or hours) while the MG importing power has relatively large load to cater within its system. Since, operating conditions in any MG may change drastically due to intermittencies involved, the tie-line schedule can therefore be changed after every 15 min intervals to adapt to the current operating scenario of the MGs.

The main contributions of this article can be summarized as follows.

1) To the best of authors knowledge, no prior work exists in the literature where a tie-line power flow control is presented for a multibus independently owned dc MGs with heterogeneous mix of sources.
2) A unified control strategy based on distributed communication is proposed to integrate the tie-line control with distributed economic dispatch and average voltage regulation.
3) The proposed philosophy not only considers the constraints of the heterogeneous power sources but also provides a methodology to achieve proper and feasible integration of different distributed control philosophies such as pinning control, distributed economic dispatch, and distributed voltage regulation.
4) Implementation of the proposed unified distributed tie-line power flow control on a real communication platform using Ethernet-based transmission control protocol/internet protocol (TCP/IP) communication.
5) Application of the proposed control philosophy for a multi-MG scenario is also demonstrated.

The remainder of the article is organized into ten sections. Section II presents the study system overview. The proposed unified hierarchical control is described in Section III. Section IV presents the results of small signal stability analysis. Section V presents the dynamic modeling and steady state analysis of the proposed hierarchical control. Simulation results under normal and faulty conditions are presented in Section VI. Analysis and performance of the system using real-time simulation and on multi-MG scenario are presented in Sections VII and VIII, respectively. The experimental validation of the proposed distributed control is presented in Section IX. Finally, Section X concludes this article.

II. System Description

The study system considered in this article is composed of two independently owned autonomous dc MGs shown in Fig. 1.

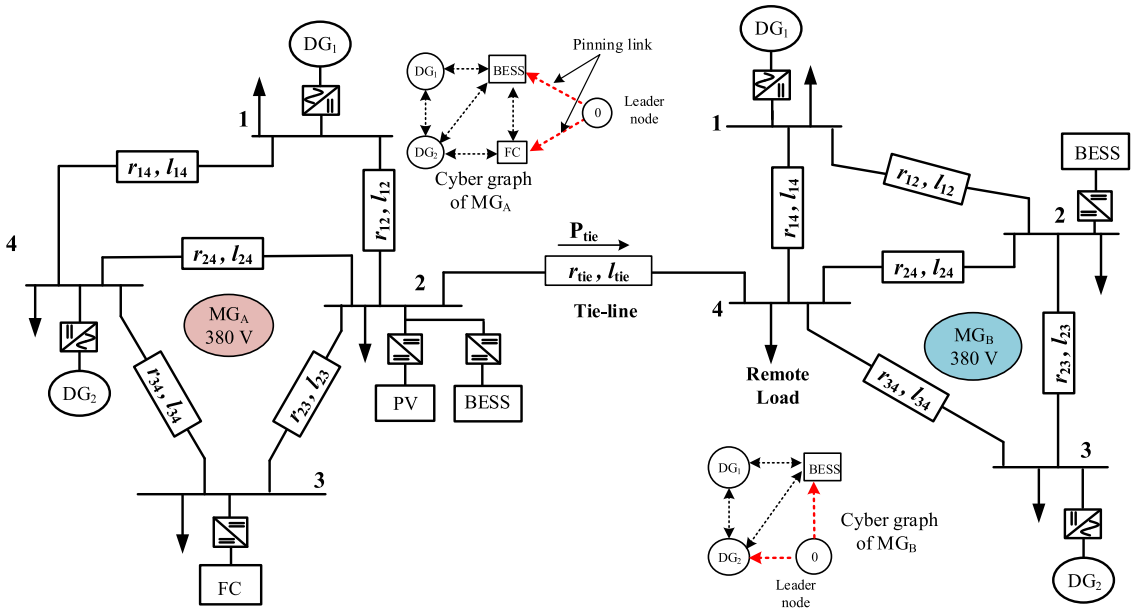

Fig. 1. Single-line diagram representation and associated cyber graphs of two independently owned dc MG clusters (MG_A and MG_B) interconnected by a tie-line.

These MGs MG_A and MG_B are interconnected to each other via tie-line. For a reliable autonomous operation, considering variable generation from PV, it is always desirable to install energy storage units in the system. Therefore, a battery energy storage system (BESS) is equipped at bus 2 of both the MGs. The nominal voltage of both MGs is 380 V. The loads connected at each bus of MGs are of constant power type, implemented using a buck dc–dc converter tightly regulating its output voltage at 120 V. Along with the BESS, three different types of sources are considered in this article namely the DG, fuel-cell, and PV plants. The total maximum generation capacities from these sources are 36 and 20 kW in MG_A and MG_B, respectively, with BESS capacities in the range of 220 V, 100 Ah in both the MGs. Maximum base load to be served in both MGs are 25 and 16 kW, respectively. Fig. 1 also shows the communication (cyber) graph for the implementation of distributed control.

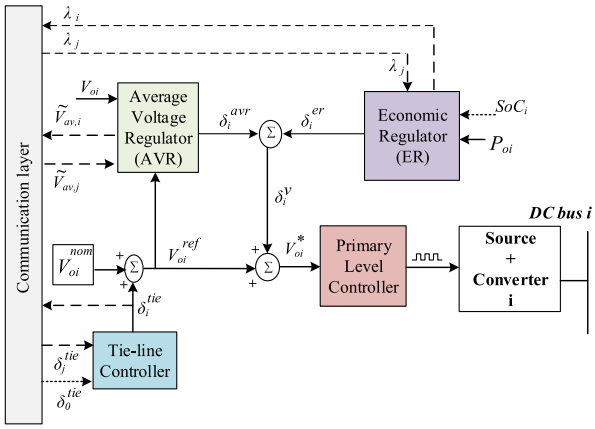

Fig. 2. Proposed distributed control schematic for an ith generator operating in VRM where $i \in$ (DG and BESS).

III. Proposed Hierarchical Control Scheme for Tie-Line Power Control

This section describes the proposed distributed control philosophy for tie-line regulation at a pre-specified level as per agreed schedule between the MGs. In an autonomous MG operation, it is desirable to have more than one unit operating in the voltage regulation mode (VRM, incorporating droop control) for smooth transition and better stability during grid and off-grid transitions [24]. However, due to heterogeneous nature of the distributed sources, the various operational constraints associated with them must also be taken into consideration. For example, the DG controller must incorporate the minimum loading limit of DG, to avoid carbon accumulation associated with low-level loading [25]. Similarly, while utilizing BESS in VRM, the SoC should also be taken into consideration to avoid deep discharge of the battery stack. While both DG and BESS are capable to handle the transients of the load, the fuel-cell unit cannot and hence, must not be subjected to load transients, as it may affect the life of fuel stack [26]. Therefore, in this article, the fuel cell unit is operated in the current control (CC) mode. The applied reference current to the fuel cell is passed through a first order delay with a time constant T_f in order to restrict the sudden change in command. Figs. 2 and 3 are the proposed control schematic corresponding to DG-BESS control and fuel-cell unit, respectively. I_0^{set} indicated in Fig. 3 corresponds to initial set current in Amps; $I_i^{\max}$ is the maximum rated current of the FC unit; while $d^{\max}$ and $d^{\min}$, respectively, represents the maximum and minimum duty ratio limit of the converter.

The control schematics present the overview of the proposed hierarchical control as applied to the respective source converter. Fig. 2 shows the operation of the converter in the VRM mode. The primary level controller receives the input voltage reference

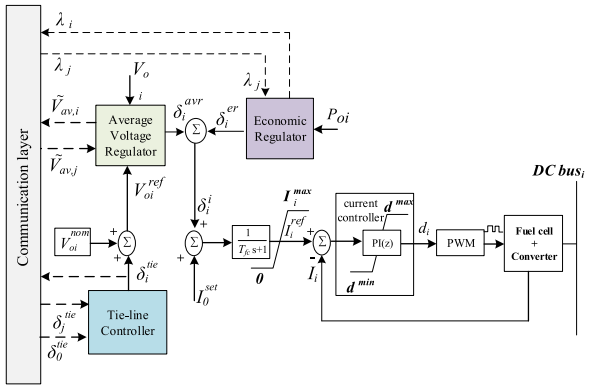

Fig. 3. Proposed distributed control schematic for the fuel-cell unit operating in the CC mode.

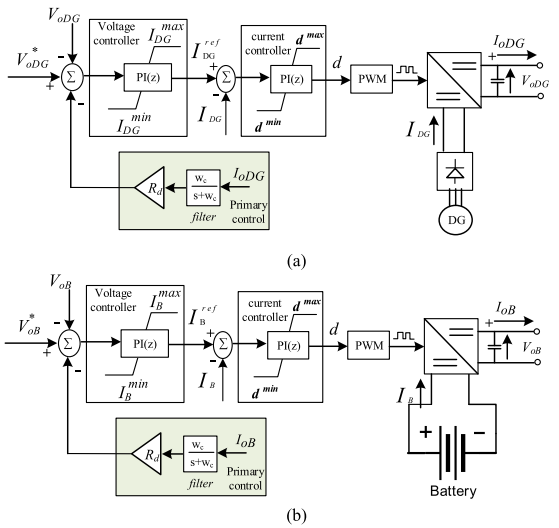

Fig. 4. Primary loop with inner voltage and CC block diagrams for: (a) DG, and (b) BESS.

from the interconnected secondary and tertiary level controllers and generates pulsewidth modulated (PWM) pulses to the source converter. This loop is the fastest to respond among others, where it is equipped with a droop-based proportional control which modifies the received voltage reference (V_{oi}^{*}), in a direction so as to share the change in load during transient conditions. V_{oi}^{nom} is the nominal voltage of the MG; V_{oi}^{ref} is the net reference commanded to the average voltage regulator (AVR) loop; and δ_i^{tie}, δ_i^{avr}, and δ_i^{er} are the voltage correction terms generated by tie-line controller, AVR and the ER, respectively. This is illustrated in detail in Fig. 4(a) and (b) which show the other intermediary stages of control such as the outer-voltage loop and the inner-current loop followed by the proportional droop control.

A. Unifying Optimization With Real-Time Voltage and Tie-Line Power Control

The preceding section explained the hierarchical framework of the control scheme wherein the interconnections and control flow among the distributed controllers was briefed. This section describes the implementation of distributed control strategy which utilizes a sparse communication network for various information exchange among the controlling nodes. The cyber graph of both MG_A and MG_B are illustrated in Fig. 1. Consensus among agents in a networked control system is a well-established area of research, where a group of nodes/agents communicate over a sparse communication network in order to reach a consensus. A simple consensus algorithm for a continuous time integrator agents can be expressed as a distributed linear consensus protocol [23] on a graph given as

$$\dot{x}_i(t) = \sum_{j \in \mathcal{N}_i} a_{ij}(x_j(t) - x_i(t)). \tag{1}$$

The outcome of the consensus protocol (29) can simply be the average of initial values, $(1/n)\sum_{i=1}^{n} x_i(0)$, where n is the total number of communicating nodes, $x_i(0)$ is the initial value, a_{ij} is an element in the adjacency matrix, $A = [a_{ij}]$ representing the associated weight for information exchanged between nodes i and j, and $\mathcal{N}_i$ is the set of neighbor nodes for the ith node. The basics of consensus in graphs is extensively covered in [23] and, hence, not covered in this article.

B. Average Voltage Regulator

The application of the dynamic consensus algorithm (DCA) for average voltage regulation is covered in [27], applied in order to regulate the network's average voltage at its rated value. The DCA protocol is employed by all the nodes and is expressed as

$$\tilde{V}_{\text{av},i} = V_{oi} + \int_0^t \sum_{j \in \mathcal{N}_i} y_{ij}(\tilde{V}_{\text{av},j} - \tilde{V}_{\text{av},i})d\tau \tag{2}$$

where, $\tilde{V}_{\text{av},i}$ is the estimated average value of node i, $\tilde{V}_{\text{av},j}$ is the estimated average value of neighboring node j, V_{oi} is the current voltage sample of node i, and y_{ij} is the weight between node i and j. Equation (2) can also be written as

$$\frac{d\gamma_i}{dt} = \sum_{j \in \mathcal{N}_i} y_{ij}(\tilde{V}_{\text{av},j} - \tilde{V}_{\text{av},i}) \tag{3}$$

$$\tilde{V}_{\text{av},i} = V_{oi} + \gamma_i \tag{4}$$

Fig. 5 shows the implementation of DCA. It can be seen that the output of DCA for an ith node is the estimated average value of the network, which is then compared with the reference voltage as set by the tie-line controller. The corresponding error is then processed by a proportional integral control which generates the voltage adjustment term δ_i^{avr}, as shown in the Fig. 5.

C. Economic Regulator

The ER is a part of secondary control which aims at minimizing the generation costs in the MG. In the traditional ac system, this problem is formulated as a classical economic dispatch problem (EDP), wherein the cost functions of the dispatchable generators are approximated as a quadratic one [28] given as

$$f_i(P_i) = a_i P_i^2 + b_i P_i + c_i \tag{5}$$

where f_i is the cost of generation for an ith generator which is a function of its output power P_i, and a_i, b_i and c_i are the coefficients of the cost function. The EDP is then solved by

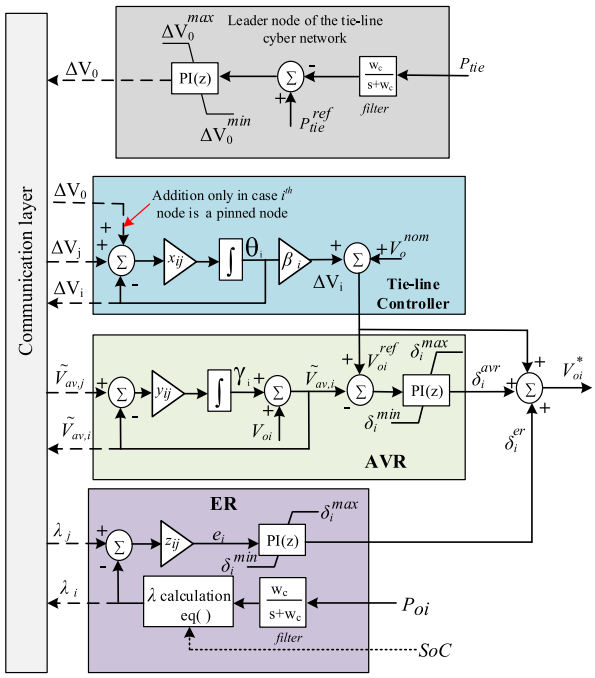

Fig. 5. Detailed control schematic of the distributed controllers highlighting the interconnections among them.

minimizing the sum of cost functions of all the dispatchable sources while satisfying generation-demand balance. Since, the cost function is a quadratic one, the solution is a stationary point where the partial derivatives of the cost function are zero. Then for the ith source, its incremental cost will be given as

$$\lambda_i = 2a_i P_i + b_i. \tag{6}$$

The implementation of the above EDP in a distributed fashion, then requires a synchronization among the nodes/agents to reach to a consensus on λ. In this article, for simplicity, it is assumed that the output power of the generators are within their limits. In case, a generator violates the upper limit, its output power is fixed at the maximum level and it does not participate any further in the EDP. Interested readers can refer to [10] for further details. The solution to the EDP depends upon the condition when the equality constraint is satisfied, i.e, the load-generation balance is satisfied. In a dc MG, the implication of load-generation mismatch is rise or fall in the dc MG voltages. Hence, if the average voltage is regulated at a reference value and is stable, then the equality constraint of the EDP is automatically met at steady state. Therefore, the AVR simultaneously generates a voltage adjustment term δ_i^{avr} in conjunction with the voltage adjustment term δ_i^{er} generated by the ER, to drive the system to an economical point while satisfying the load-generation balance.

The cost functions and incremental costs of DG and FC are formulated as follows:

$$F_{\text{DG}} = a_{\text{DG}} P_{\text{DG}}^2 + b_{\text{DG}} P_{\text{DG}} + c_{\text{DG}} \tag{7}$$

$$\lambda_{\text{DG}} = 2a_{\text{DG}} P_{\text{DG}} + b_{\text{DG}} \tag{8}$$

$$F_{\text{FC}} = a_{\text{FC}} P_{\text{FC}}^2 + b_{\text{FC}} P_{\text{FC}} + c_{\text{FC}} \tag{9}$$

$$\lambda_{\text{FC}} = 2a_{\text{FC}} P_{\text{FC}} + b_{\text{FC}} \tag{10}$$

where F_{DG} and P_{DG} are the cost function and output power of DG, respectively, while F_{FC} and P_{FC} are the cost function and output power of fuel-cell unit, respectively. The a, b, and c parameters with subscripts DG and FC are the associated cost-coefficients corresponding to DG and FC, respectively. λ_{DG} and λ_{FC} are the incremental cost of DG and FC, respectively. For the BESS, a general cost function [29] is modified to be made compatible with the cost function of DG and FC. It is quadratic and takes into account the SoC of battery given as

$$F_B = a_B \left(P_B + 6P_B^{\max}(1 - \text{SoC})\right)^2 + b_B \left(P_B + 6P_B^{\max}(1 - \text{SoC})\right) + c_B \tag{11}$$

$$\lambda_B = a_B \left(2P_B - 6P_B^{\max}(\text{SoC} - 1)\right) + b_B \tag{12}$$

where F_B is the designed fuel cost function for the BES which is a function of BESS operating power P_{BES} (in kW) and SoC. $P_B^{\max}$ is the allowable maximum power of BESS (in kW). λ_B is the incremental cost of BESS, and a_B, b_B and c_B are the coefficients of the cost function.

The implementation of distributed economic dispatch as an ER is shown in Fig. 5. As shown, the ith ER employs a local voting protocol, to generate a neighborhood error term. This error term is then processed by a proportional-integral (PI) controller which generates a voltage adjustment term δ_i^{er}, as shown in the Fig. 5

$$\frac{d\zeta_i^{\text{er}}}{dt} = \sum_{j \in \mathcal{N}_i} z_{ij}(\lambda_j - \lambda_i) \tag{13}$$

$$\delta_i^{\text{er}} = K_p^{\text{er}} \left(\sum_{j \in \mathcal{N}_i} z_{ij}(\lambda_j - \lambda_i) \right) + K_i^{\text{er}} \zeta_i^{\text{er}} \tag{14}$$

where λ_i and λ_j are the incremental costs of ith and jth unit, respectively, $z_{i,j}$ is the communication weight, ζ_i^{er} is a state variable of the ER corresponding to the integral term, and K_p^{er} and K_i^{er} are the proportional and integral gains, respectively.

D. Tie-Line Controller

The distributed pinning control strategy presented in [30], is applied in this article to regulate the power flow in the tie-line. The pinning strategy is a special case of centralized control where instead of communicating the information to all the nodes in the network, only few nodes are selected or pinned to diffuse the information among rest of the nodes. This reduces the cost of transmission and improves the reliability of the system. The nodes are generally classified as pinning node/leader node and pinned nodes. The objective of applying pinning strategy for tie-line control is to make the various sources in the network, participate in regulating the tie-line power at a desired level. It is similar to the automatic generation control, where the raw area control error is transmitted to various participating units for load frequency and tie-line power control. In our case, the boundary bus is chosen as a leader node which is responsible for locally measuring the tie-line power and based on the error processed by a PI controller, it generates a voltage adjustment term (ΔV_0) to be pinned to neighboring nodes at buses 3 and 4, as shown in the study system. These nodes are therefore termed as pinned

nodes whose dynamic can be represented as [30]

$$\frac{d\theta_i}{dt} = \sum_{j\in\mathcal{N}, j\neq 0} x_{i,j}(\Delta V_j - \Delta V_i) + x_{i0}(\Delta V_0 - \Delta V_i) \quad (15)$$

$$\Delta V_i = \beta_i \theta_i \quad (16)$$

where

$$\Delta V_0 = K_p^{P_{\text{tie}}}(P_{\text{tie}}^{\text{ref}} - P_{\text{tie}}) + \int K_i^{P_{\text{tie}}}(P_{\text{tie}}^{\text{ref}} - P_{\text{tie}})dt. \quad (17)$$

The term ΔV_i, is then added with nominal voltage of the system (V_o^{nom}) to generate the reference average voltage (V_{oi}^{ref}) which is then compared with estimated average voltage of the ith converter to generate an error which is processed by the AVR, as shown in the Fig. 5. This can be expressed as

$$V_{oi}^{\text{ref}} = V_o^{\text{nom}} + \Delta V_i \quad (18)$$

$$\frac{d\zeta_i^{\text{avr}}}{dt} = V_{oi}^{\text{ref}} - \tilde{V}_{\text{av},i} \quad (19)$$

$$\delta_i^{\text{avr}} = K_p^{\text{avr}}(V_{oi}^{\text{ref}} - \tilde{V}_{\text{av},i}) + K_i^{\text{avr}}\zeta_i^{\text{avr}} \quad (20)$$

where ζ_i^{avr} is a state variable of the AVR corresponding to the integral term, and K_p^{avr} and K_i^{avr} are the corresponding proportional and integral gains, respectively. Finally, the reference voltage to primary control level can be obtained as

$$V_{oi}^{*} = V_{oi}^{\text{ref}} + \delta_i^{\text{avr}} + \delta_i^{\text{er}}. \quad (21)$$

IV. Small Signal Stability Analysis

The objective of this section is to investigate the small signal behaviour of the studied system shown in Fig. 1. Specifically the impact of variations in communication weights and tie-line controller gain on the small-signal stability is studied. Detailed modeling of the various subsystems is carried out in order to study the interaction among different components of the system. The study system can be broadly classified as converter and its control, communication system, and network. The following subsection presents the modeling approach for a converter, i in VRM.

A. Modeling of ith Converter and Control in VRM

A boost converter is employed which interfaces the respective source with the network. Its differential equations (DE), based on the circuit averaging technique, can be given as

$$L_i\frac{di_{Li}}{dt} = V_i^{in} - (1-d_i)V_{oi} - i_{Li}r_i \quad (22)$$

$$C_i\frac{dV_{oi}}{dt} = i_{Li}(1-d_i) - \frac{P_i^{\text{cpl}}}{V_{oi}} - i_{ij}\forall j = 1 \text{ to } n, j \neq i \quad (23)$$

where v_i^{in}, V_{oi}, and i_{Li} are input voltage, output voltage, and input inductor current, respectively. C_i, L_i, and r_i are the output capacitance, input inductance and resistance, respectively. d_i is the duty ratio, P_i^{cpl} is the input power of the connected constant power load (CPL) at the operating point, i_{ij} is the network current, and n is the number of branches interconnected with ith bus. The primary level and hierarchical level differential can be expressed as

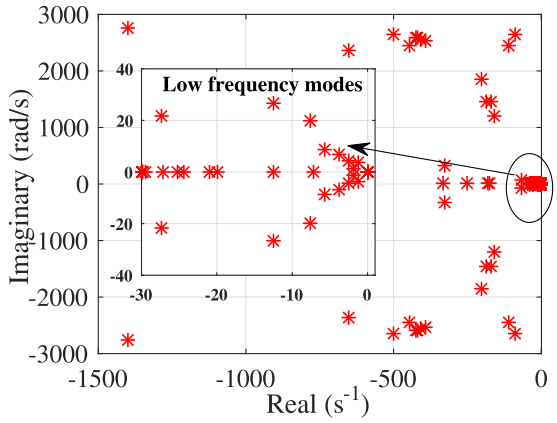

Fig. 6. Eigenvalues of the complete system.

$$\frac{d\phi_{vi}}{dt} = V_{oi}^{*} - R_d\tilde{i}_{oi} - V_{oi} \quad (24)$$

$$\frac{d\phi_{ci}}{dt} = i_{Li}^{*} - i_{Li} \quad (25)$$

$$\frac{d\tilde{i}_{oi}}{dt} = w_c(1-d_i)i_{Li} - w_c\tilde{i}_{oi} \quad (26)$$

$$L_{ij}\frac{i_{ij}}{dt} = V_{oi} - V_{oj} - i_{ij}r_{ij} \quad (27)$$

where ϕ_{vi} is the primary level voltage controller, R_d is the droop coefficient, $\tilde{i}_{oi}$ is the low pass filtered output current, ϕ_{ci} is the inner current controller, i_{Li}^{*} is the reference current for the inner current loop, w_c is the cutoff frequency of the low pass filter, and L_{ij} and r_{ij} are the network line inductance and resistance, respectively, between the ith and jth bus. Equations (23)–(27) along with (4), (14), (16), and (20) constitute the model of ith converter operating in VRM. Proceeding in a similar way for other converters in both MGs, results in a total of 84 DE. These DE are linearized around an operating point obtained from simulation. The operating point constitutes a snapshot when tie-power export from MG_A to MG_B is regulated at 4 kW. Finally, the closed-loop state space model is obtained by eliminating the intermediary and auxiliary variables as follows:

$$\dot{\Delta x} = A_{\text{sys}_{(84\times 84)}}\Delta x. \quad (28)$$

The results of the small signal model is presented in Fig. 6, which shows the graphical representation of all the eigenvalues while Table I shows the tabular presentation of critical modes along with information of the states participating in them. The participating states in various modes are obtained through a participation matrix. It can be seen that all the states are negative and appearing in the left half plane, validating a stable operating point. Moreover, conclusions drawn from the participation analysis reveal that most of the low frequency modes are controller modes. It can also be noticed that ER loop (ζ^{er}) participates exclusively in all the low frequency modes along

TABLE I
CRITICAL EIGENVALUES AND DOMINANT STATE VARIABLES

λ	Eigenvalue	Dominant states
$\lambda_{1,2}$	-12.405 $\pm$ 26.659j	ζ_{1b}^{er} (23.78%), ζ_{2b}^{er} (13.57%), $\tilde{P}_{1b}$ (23.05%), ϕ_{v1b} (15.47%), $\tilde{P}_{3b}$ (8.46%)
$\lambda_{3,4}$	-27.288 $\pm$ 21.55j	V_{oia} (18.8%), ϕ_{via} (18.214%) V_{oib} (18.8%), ϕ_{vib} (18.05%)
$\lambda_{5,6}$	-7.52$\pm$ 20.05j;	ζ_{3b}^{er} (23.45%), $\tilde{P}_{3b}$ (10.89%), ζ_{2b}^{er} (13.82%), $\tilde{P}_{2b}$ (11.84%), ϕ_{2b} (18.46%)
$\lambda_{7,8}$	-5.667$\pm$ 8.597j	ζ_{1a}^{er} (15.23%), ζ_{3a}^{er} (23.91%), ϕ_{v1a} (17.18%), ϕ_{v4a} (24.9%)
$\lambda_{9,10}$	-3.725 $\pm$ 7.104j	ζ_{1a}^{er} (12.75%), ζ_{4a}^{er} (21.387%), ζ_{2a}^{er} (8.77%), ϕ_{v2a} (22.33%), ϕ_{v1a} (13.19%),ϕ_{v4a} (7.73%)
$\lambda_{11,12}$	-2.494 $\pm$ 4.613j	ζ_{2a}^{er} (8.77%), ζ_{4a}^{er} (6.47%), ϕ_{v2a} (10.01%), ϕ_{v2b} (7.74%)
$\lambda_{13,14}$	-1.148 $\pm$ 3.903j	I_{3a}^{delay} (26.05 %), ζ_{2a}^{er} (18.46%), ζ_{3a}^{avr} (10.45%)
$\lambda_{15,16}$	-1.77 $\pm$ 1.548j	ζ_{0}^{tie} (34.14%), θ_i (35.75%)

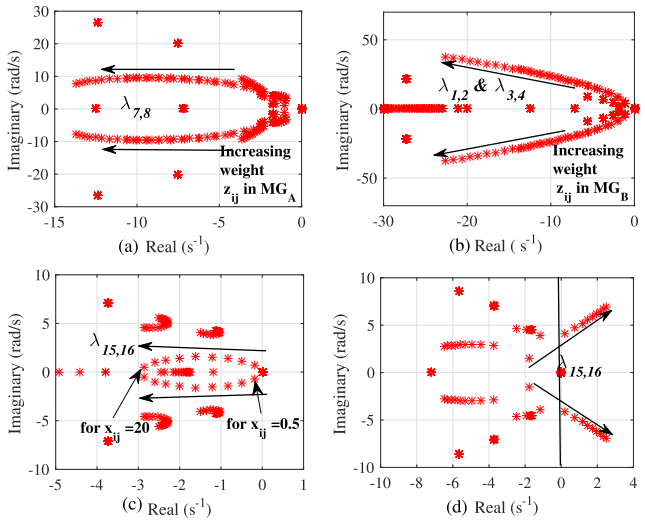

Fig. 7. Responses of eigenvalue trajectories for: (a) variation in communication weight, z_{ij} of MG_A from 0.5 to 20; (b) variation in communication weight, z_{ij} of MG_B from 1 to 20; (c) variation in communication weight, x_{ij} of the tie-line controller from 1 to 20; and (d) variation in integral gain of the tie-line leader node from 0.0021 to 0.05.

with the primary level voltage controller (ϕ_v). Therefore, the effect of variations in communication weights of ER and tie-line controller is investigated below. The eigenvalue trajectories of various modes are presented in Fig. 7. From the participation analysis presented in Table I, we can notice that states of ER in MG_A, i.e., ζ_i^{er} from (14), participate in low frequency modes such as $\lambda_{7,8}$, $\lambda_{9,10}$, $\lambda_{11,12}$, and $\lambda_{13,14}$. Since, the communication weight, z_{ij}, links the various converters in system, its effect on these modes trajectory is shown in Fig. 7(a). It can be seen that, by increasing the gain z_{ij} from 0.5 to 20, the eigenvalues $\lambda_{7,8}$ show most sensitivity among the others. It can be seen

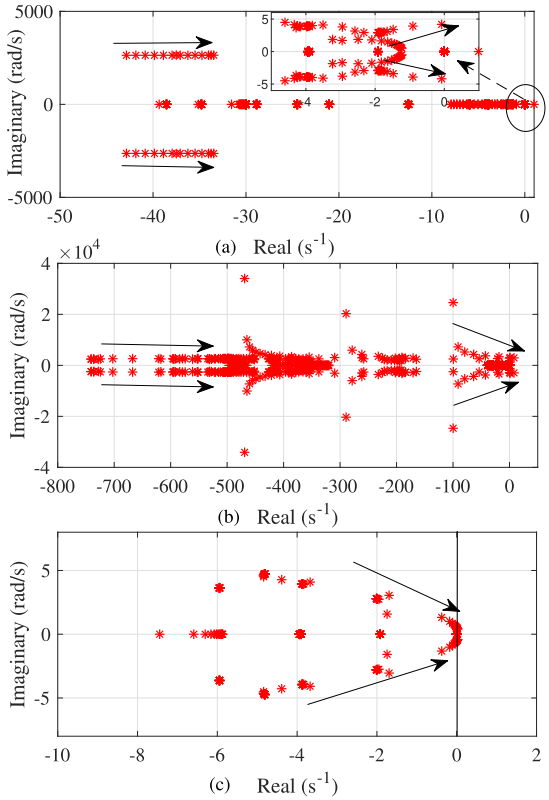

Fig. 8. Responses of eigenvalue trajectories for: (a) variation in in tie-line resistance and inductance from 0.9879 to 0.0329 Ω and 1.5 to 50 μH, (b) variation in network resistance and inductance in MGA from three times the base value to one percent of the base value. (c) Response of low-frequency critical modes with increasing communication delay from 0.01 s to 1.2 ms.

that with increasing z_{ij}, the damping of $\lambda_{7,8}$ increases as it moves further deep in the left-half of s-plane. This is due to the increase in convergence speed of consensus as communication weight increases for the ER loop. Similarly, increasing other communication weights exhibits similar responses shown in Fig. 7(b) and (c). Since, the control of tie-line power flow is placed at the top most level of control hierarchy, the control gains have to be selected carefully such that it exhibits an optimal transient response, i.e., neither too fast nor too slow. The time domain response of this control is dependent on the leader node's integral gain. The effect of this integral gain is highlighted in Fig. 7(d), where the eigenvalue, $\lambda_{15,16}$ crosses the origin and moves into right half as the gain increases from 0.0021 to 0.05. Hence, this results in a clear tradeoff between speed of response and stability. A small value can lead to a slow time response while a large value can lead to instability. Therefore, the integral gain of 0.0021 is selected as an optimal one.

Fig. 8(a) shows the eigenvalue trajectory response to variation in tie-line parameters, while Fig. 8(b) shows the effect due to variation in network parameters of MG_A. It can be inferred from both the responses that stability of the system is weakened as the resistance and inductance values are decreased. Particularly, as the resistance decreases, the damping in the network also reduces which evidently leads to reduction in the stability margin of the system.

Fig. 8(c) shows the eigenvalue trajectory response of the small signal system when communication time delay in channel 2–3 of the tie-line cyber graph is increased from 0.01 to 1.5 s. It can be seen from the figure that as the time-delay increases, the low frequency modes of the small signal system drifts to the right side of the *s*-plane. At a critical time-delay of 1.1 s, the low frequency modes corresponding to $\lambda_{15,16}$ and $\lambda_{11,12}$ touches the imaginary axis. Hence, it can be concluded from the analysis, that the stability of the system can be maintained up to a theoretical maximum communication delay of 1.1 s. The small signal modeling considering the communication delay is presented in the Appendix.

V. Dynamic Modeling and Steady State Analysis of Distributed Controllers

This section presents the dynamic modeling of the distributed consensus algorithms followed by steady state analysis to prove the existence of an equilibrium point satisfying the different objectives of hierarchical control.

The voltage shift due to ER in frequency domain can be written as

$$\delta^{\mathrm{ER}} = -G^{\mathrm{ER}} L_N \Lambda \tag{29}$$

where, δ^{ER} and Λ are the Laplace transforms of $\delta^{\mathrm{er}} = [\delta_1^{\mathrm{er}} \cdots \delta_N^{\mathrm{er}}]$ and $\lambda = [\lambda_1 \cdots \lambda_N]$, respectively; $G^{\mathrm{ER}} = \mathrm{diag}\{G_i^{\mathrm{er}}(\mathrm{s})\} \in \mathbb{R}^{\mathrm{N}\times\mathrm{N}}$ is the PI controller matrix of the ER. The incremental cost of the source $'i'$ can be defined as

$$\lambda_i = b_i + 2a_i p_i \tag{30}$$

$$\lambda = B + 2AP \tag{31}$$

where $B = [b_1 \cdots b_N]^T \in \mathbb{R}^{\mathrm{N}\times 1}$ and $A = \mathrm{diag}\{a_i\} \in \mathbb{R}^{\mathrm{N}\times\mathrm{N}}$. In the frequency domain, (31) can be written as

$$\Lambda = B + 2AP \tag{32}$$

where P and $B = B/s$ are the Laplace transforms of B and P, respectively. Substituting (32) in (29), we get

$$\delta^{\mathrm{ER}} = -G^{\mathrm{ER}} L_N (B + 2AP). \tag{33}$$

Now the voltage shift due to AVR can be written as

$$\bar{V}_{\mathrm{av}} = s(sI_N + cL)^{-1} V_0 = G_{\mathrm{est}} V_0 \tag{34}$$

where $\bar{V}_{\mathrm{av}}$ and V_0 are the Laplace transforms of $\bar{v}_{\mathrm{av}} = [\bar{v}_{\mathrm{av1}} \cdots \bar{v}_{\mathrm{av}N}]^T$ and $v_0 = [v_{01} \cdots v_{0^{\cdot}N}]^T \in \mathbb{R}^{\mathrm{N}\times 1}$, respectively. I_N and G_{est} are the identity matrix and the voltage estimator transfer function, respectively. In frequency domain (34) can be written as

$$\delta^{\mathrm{avr}} = G^{\mathrm{avr}}(V_0^{\mathrm{REF}} - \bar{V}_{\mathrm{av}}) = G^{\mathrm{avr}}(V_0^{\mathrm{ref}} - G_{\mathrm{est}} V_0) \tag{35}$$

where δ^{avr} and V_0^{REF} are the Laplace transforms of $\delta^{\mathrm{avr}} = [\delta_1^{\mathrm{avr}} \cdots \delta_N^{\mathrm{avr}}]^T$ and $V_0^{\mathrm{ref}} = [V_{01}^{\mathrm{ref}} \cdots V_{0N}^{\mathrm{ref}}]^T \in \mathbb{R}^{\mathrm{N}\times 1}$, respectively, and $G^{\mathrm{avr}} = \mathrm{diag}\{G_i^{\mathrm{avr}}(s)\} \in \mathbb{R}^{\mathrm{N}\times\mathrm{N}}$ is the AVR controller matrix. The voltage shift due to the tie-line controller is added to the system nominal voltage (V_0^{nom}), which becomes the final voltage reference to the AVR. Equation (16) can be written in frequency domain as

$$\delta^{\mathrm{TIE}} = (X - DI_N)\Delta V \tag{36}$$

where δ^{tie} and ΔV are the Laplace transforms of $\delta^{\mathrm{tie}} = [\delta_1^{\mathrm{tie}} \cdots \delta_N^{\mathrm{tie}}]^T$ and $\Delta V = [\Delta V_1 \cdots \Delta V_N]^T \in \mathbb{R}^{\mathrm{N}\times 1}$, respectively. Then

$$V_0^{\mathrm{REF}} = V_0^{\mathrm{nom}} + \delta^{\mathrm{TIE}} \tag{37}$$

$$V_0^{\mathrm{REF}} = V_0^{\mathrm{nom}} + (X - DI_N)\Delta V. \tag{38}$$

Substituting (38) in (35), we get

$$\delta^{\mathrm{AVR}} = G^{\mathrm{AVR}}(V_0^{\mathrm{nom}} + (X - DI_N)\Delta V - G_{\mathrm{est}} V_0. \tag{39}$$

The final voltage command (V_0^*) can now be written

$$V_0^* = V_0^{\mathrm{nom}} + (X - DI_N)\Delta V + \delta^{\mathrm{avr}} + \delta^{\mathrm{ER}}. \tag{40}$$

Equation (40) is the voltage command for generator operating in VRM. Similarly, for the fuel-cell unit operating in the CC mode, the current command can be written as

$$I_0^* = I_0^{\mathrm{set}} + \delta^{\mathrm{avr}} + \delta^{\mathrm{ER}}. \tag{41}$$

The overall system model can be obtained in matrix form as

$$V_0 = G_{\mathrm{cl}}^{\mathrm{VR}} V_0^* + G_{\mathrm{cl}}^{\mathrm{CC}} I_0^*. \tag{42}$$

where V_0 is the Laplace transform of the system bus voltages, $v_o = [v_{01} v_{02}]^T$; $G_{\mathrm{cl}}^{\mathrm{VR}}$ and $G_{\mathrm{cl}}^{\mathrm{CC}}$ represents the closed-loop transfer function matrices of converters in VRM and CC mode, respectively. The system admittance matrix Y relates the source currents to the bus voltages as

$$I_0 = YV_0. \tag{43}$$

The relation between vector of source output powers to vectors of output voltage and currents cannot be directly found because of the involved multiplication. However, small perturbation of source power can be used to derive the relation as follows:

$$\tilde{p}_{0i} = \bar{V}_{0i}\tilde{i}_{0i} + \tilde{v}_{0i}\bar{I}_{0i} \tag{44}$$

where $\bar{V}_{0i}$ and $\bar{I}_{0i}$ are the output voltage and current of source i around the operating point, respectively, and $\tilde{v}_{0i}$ and $\tilde{i}_{0i}$ are the perturbations, respectively. Assuming that the current perturbations to be larger than that of the voltage, (44) can be approximately written as

$$\tilde{p}_{0i} \approx \bar{V}_{0i}\tilde{i}_{0i}. \tag{45}$$

The output voltage of source i at the operating point can be considered as the nominal voltage of the MG, V_{nom}. Then (45) can be written as

$$\tilde{p}_{0i} = V_{\mathrm{nom}}\tilde{i}_{0i}. \tag{46}$$

Using (36), (39), (40), and (46), we can write

$$\begin{aligned} V_0^* = {} & V_0^{\mathrm{nom}} + (X - DI_N)\Delta V + G^{\mathrm{avr}}(V_0^{\mathrm{nom}} \\ & + (X - DI_N)\Delta V - G_{\mathrm{est}} V_0) \\ & - G^{\mathrm{ER}} L_N (B + 2AV_{\mathrm{nom}} I_0) \end{aligned} \tag{47}$$

and

$$\begin{aligned} I_0^* = {} & I_0^{\mathrm{set}} + G^{\mathrm{avr}}(V_0^{\mathrm{nom}} + (X - DI_N)\Delta V \\ & - G_{\mathrm{est}} V_0) - G^{\mathrm{ER}} L_N (B + 2AV_{\mathrm{nom}} I_0). \end{aligned} \tag{48}$$

We can define $C \triangleq 2AV_{\text{nom}}$ and using (43) we can write (47) and (48) as

$$V_0^* = V_0^{\text{nom}} + (X - DI_N)\Delta V + G^{\text{avr}}(V_0^{\text{nom}} + (X - DI_N)\Delta V - G_{\text{est}}V_0) - G^{\text{ER}}L_N(B + CYV_0) \quad (49)$$

$$I_0^* = I_0^{\text{set}} + G^{\text{avr}}(V_0^{\text{nom}} + (X - DI_N)\Delta V - G_{\text{est}}V_0) - G^{\text{ER}}L_N(B + CYV_0). \quad (50)$$

Substituting (49) and (50) in (42), we get

$$V_0 = G_{\text{cl}}^{\text{VR}}[V_0^{\text{nom}} + (X - DI_N)\Delta V + G^{\text{avr}}(V_0^{\text{nom}} + (X - DI_N)\Delta V - G_{\text{est}}V_0) - G^{\text{ER}}L_N(B + CYV_0)] + G_{\text{cl}}^{\text{CC}}[I_0^{\text{set}} + G^{\text{avr}}(V_0^{\text{nom}} + (X - DI_N)\Delta V - G_{\text{est}}V_0) - G^{\text{ER}}L_N(B + CYV_0)]. \quad (51)$$

Rearranging for V_0, we can obtain

$$V_0 = [I_N + G^{\text{avr}}G_{\text{cl}}^{\text{VR}}G_{\text{est}} + G_{\text{cl}}^{\text{VR}}G^{\text{ER}}L_NCY + G_{\text{cl}}^{\text{CC}}G^{\text{avr}}G_{\text{est}}]^{-1} \times G_{\text{cl}}^{\text{VR}}[V_0^{\text{nom}} + (X - DI_N)\Delta V + G^{\text{avr}}] + G_{cl}^{\text{CC}}[I_0^{\text{set}} + G^{\text{avr}}(V_0^{\text{nom}} + (X - DI_N)\Delta V - G_{\text{est}}V_0) - G^{\text{ER}}L_NB(G_{\text{cl}}^{\text{CC}} + G_{\text{cl}}^{\text{VR}})]. \quad (52)$$

By applying the final value theorem to (52), the steady state bus voltages can be obtained as

$$V_0^{\text{ss}} = \lim_{s\to 0} sV_0 \quad (53)$$

$$V_0^{\text{ss}} = \lim_{s\to 0}(sI_N + sG^{\text{avr}}G_{\text{cl}}^{\text{VR}}G_{\text{est}} + sG_{\text{cl}}^{\text{VR}}G^{\text{ER}}L_NCY + sG_{\text{cl}}^{\text{CC}}G^{\text{avr}}G_{\text{est}}]^{-1} \times sG_{\text{cl}}^{\text{VR}}[V_0^{\text{nom}} + (X - DI_N)\Delta V + G^{\text{avr}}] + sG_{\text{cl}}^{\text{CC}}[I_0^{\text{set}} + sG^{\text{avr}}(V_0^{\text{nom}} + (X - DI_N)\Delta V - G_{\text{est}}V_0) - G^{\text{ER}}L_NB(G_{\text{cl}}^{\text{CC}} + G_{\text{cl}}^{\text{VR}})]. \quad (54)$$

The controller matrices G^{avr} and G^{ER} are diagonal PI matrices and can be written as $G^{\text{avr}} = G_P^{\text{avr}} + G_I^{\text{avr}}s^{-1}$ and $G^{\text{ER}} = G_P^{\text{ER}} + G_I^{\text{ER}}s^{-1}$, where G_P^{avr}, G_I^{avr}, G_P^{ER}, and G_I^{ER} are constant diagonal matrices carrying the proportional and integral gains of the controllers. Further, the dc gains of $G_{\text{cl}}^{\text{VR}} = G_{\text{cl}}^{\text{CC}} = 1_N$. In addition, the limit $\lim_{s\to 0} G_{\text{est}} = Q_N$, where $Q_N \in \mathbb{R}^{\text{N}\times\text{N}}$ is the averaging matrix, whose entries are all $1/N$. Equation (54) can now be simplified as

$$V_0^{\text{ss}} = (2 * G_I^{\text{avr}}Q_N + G_I^{\text{ER}}L_NCY)^{-1} \times 2 * G_I^{\text{avr}}(V_0^{\text{nom}} + (X - DI_N)\Delta V) - G^{\text{ER}}L_NB \quad (55)$$

$$(2 * G_I^{\text{avr}}Q_N + G_I^{\text{ER}}L_NCY)V_0^{\text{ss}} = 2 * G_I^{\text{avr}}(V_0^{\text{nom}} + (X - DI_N)\Delta V) - G^{\text{ER}}L_NB. \quad (56)$$

Given Q_N, D, and L_N and since $L_N$is balanced, we can conclude that $Q_NL_N = 0$ and $Q_ND = 0$. Therefore, pre-multiplying both sides of (56), we can obtain

$$Q_N(2 * G_I^{\text{avr}}Q_N)V_0^{\text{ss}} = Q_N * 2 * G_I^{\text{avr}}(V_0^{\text{nom}} + (X - DI_N)\Delta V). \quad (57)$$

In addition, according to the definition of the averaging matrix, $Q_NV_0^{\text{ss}} = \underline{1}\langle V_0^{\text{ss}}\rangle$, where the scalar $\langle V_0^{\text{ss}}\rangle$ is the average of the elements of V_0^{ss} at steady state. Hence, (57) can be written as

$$Q_N2 * G_I^{\text{avr}}\langle V_0^{ss}\rangle = Q_N2 * G_I^{\text{avr}} * V_0^{\text{ref}} \quad (58)$$

where V_0^{ref} is the net reference obtained from the addition of V_0^{nom} and voltage shift term generated by the tie-line controller. Now, since $Q_N * 2 * G_I^{\text{avr}}$ is a nonzero vector, we can conclude that $\langle V_0^{\text{ss}}\rangle = V_0^{\text{ref}}$. In other words, the average of the output voltages is equal to the net reference set by hierarchical control. This concludes the equilibrium analysis of the proposed unified distributed consensus algorithm.

VI. Simulation Results and Discussion

Two 380-V nonidentical dc MGs, shown in Fig. 1, were developed in MATLAB/Simulink to evaluate the performance of the proposed tie-line controller. The MGs are composed of PV, battery banks, DG sets and loads, distributed at different buses of each MG. To interface these sources with the MG network, power electronic converters are used. For instance, PV is interfaced using a boost converter operating in maximum power point tracking (MPPT) mode. Further, battery banks are connected through synchronous buck converters to enable bidirectional power flow whereas DGs are connected using a voltage source converter. Additionally, CPLs are considered in this article. Electrical specifications of the two MG system and converters' parameters and cost-function coefficients are given in Table II. Three different case studies have been presented to evaluate the performance of the proposed control scheme as described below:

A. Case-1: Controller Performance Under Normal Operation

In this case, the performance of the tie-line controller is evaluated under normal operation. Initially, the tie-line controller was disabled and the tie-line was unregulated while the AVR and the ER loop were enabled, maintaining the average voltage and optimal operation, respectively, in the MGs, as shown in Fig. 9. Before the instant $t = t_1$, the power flow P_{tie} was equal to 2 kW. At $t = t_1$, a step change in PV insolation was introduced in MG_A, causing a reduction in PV power output from 4.72 to 2.3 kW as shown in Fig. 9(b). In a dc network, changes in power distribution causes changes in bus voltages. Hence, after t_1, as the power distribution in MG_A changes, its boundary bus voltage (V_4) reduces, causing a reduction in power exported to MG_B. The power flow, P_{tie} was however minimal (0.14 kW) due to AVR action in both MGs as the average voltages in both MGs are nearly same at 380 V, as seen from Fig. 9(d). It is intuitive, that without the AVR action, a relatively large voltage deviations will occur in the network, which can cause larger deviations in tie-line power flow from its scheduled value.

TABLE II
SIMULATION PARAMETERS

Element	Technical Parameter	Specifications
PV	V_{mp} , I_{mp}, Rated power at $1000W/m^2$	164.1 V, 61.38 A 10 kW
BESS Stack	Capacity Nominal voltage	50 Ah 220 V
PEMFC	Cell Voltage, No. of series cells Open circuit voltage Rated power Current reference delay (T_f)	1.229 V 160 194.64 V 10 kW 0.5 s
DC-DC Converter	Nominal output voltage, v_o Input filter, (r, L) Output Capacitance, C	380 V DC 0.2 Ω, 4 mH 4700 μ F
Primary Controllers	Outer voltage loop (K_p,K_i) Inner current loop (K_p,K_i) Droop gain, (R_d)	0.5,10 0.01,75 0.25
AVR	K_p^{avr}, K_i^{avr},y_{ij}	0.4,10,10
ER(MG_A)	K_p^{er}, K_i^{er},z_{ij}	0.15,2,5
ER(MG_B)	K_p^{er}, K_i^{er},z_{ij}	0.1,6,10
Tie-Line Controller	K_p^{tie}, K_i^{tie}, x_{ij}	0.00048,0.0021,5
Network parameters	r_{12}, L_{12}, r_{14}, L_{14}, r_{23}, L_{23}, r_{24}, L_{24}, r_{34}, L_{34}	0.07 Ω & 0.1 mH, 0.05 Ω & 0.4 mH, 0.06 Ω & 0.2 mH, 0.04 Ω & 0.3 mH, 0.02 Ω & 0.1 mH
Cost Coefficients MG_A	a_1, b_1, c_1 a_2, b_2, c_2 a_3, b_3, c_3 a_4, b_4, c_4	0.9,0.1,6.4 0.28,0.08,4 0.95,0.13,7.4 0.73,0.08,6
Cost Coefficients MG_B	a_1, b_1, c_1 a_2, b_2, c_2 a_3, b_3, c_3	1.1,0.15,6 0.04,0.08,4.5 0.77,0.05,6.2

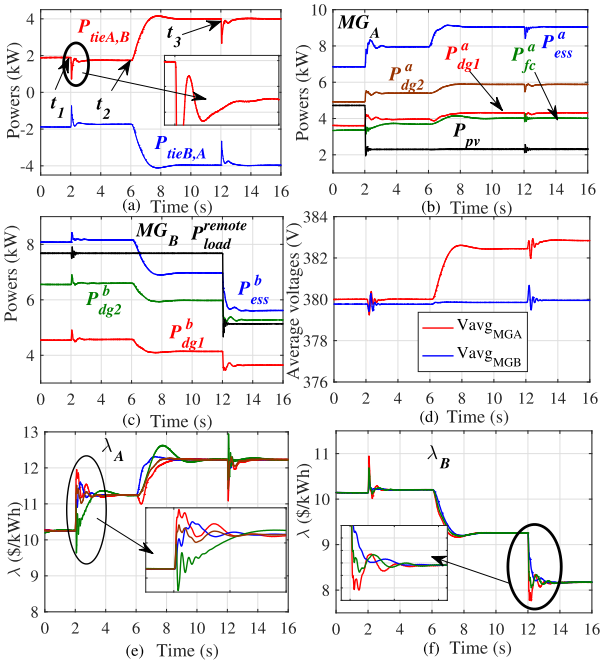

Fig. 9. Simulation results of case-1. (a) Tie-line power. (b) MG_A powers. (c) MG_B powers. (d) Average voltages of both MGs. (e) Incremental costs of MG_A. (f) Incremental costs of MG_B.

At $t = t_2$, tie-line controller was enabled and a tie-line power reference of 4 kW was given to send power from MG_A to MG_B. The power flow, P_{tie} slowly increases and with a slight overshoot, it tracks the reference value in approximately 4 s, as shown in Fig. 9(a). Since only MG_A exercises tie-line control, the average voltage of MG_B remains unaltered while that of MG_A experiences a change of approximately 2.5 V, as shown in Fig. 9(d) in order to push power through the tie-line. Moreover, it can be noted that during both the events t_1 and t_2, the fuel cell power changes slowly, while the transients were absorbed by the remaining sources.

To further test the efficacy of the tie-line controller, a step reduction in remote load was introduced in MG_B at $t = t_3$, as shown in the power figures in Fig. 9(c). It can be seen that after a transient, the P_{tie} was settled at the reference value. An important implication of this can be observed from Fig. 9(b) and (c) where the load disturbance in MG_B was not reflected in MG_A in steady state, due to the regulated tie-line. Further, in the performance of ER, as illustrated in Fig. 9(e) and (f), the incremental costs in both MGs (λ_A and λ_B) were equal despite various disturbances.

B. Case-2: Effect of ER on the Tie-Line Controller

This case illustrates the effect of ER on the tie-line controller and on the system responses. It also highlights the decoupling among different controllers such as AVR, ER, and tie-line controller, due to their different time-scale of operation. In this case, initially the tie-line controller and AVR were enabled and ER in both MGs were disabled. The tie-line power, P_{tie} was regulated at 4 kW when at $t = t_1$, the ER of MG_A was first enabled, as shown in Fig. 10(d). The incremental costs of the different generators reach a consensus in about 1.5 s and settle at a value of 11.6 \$/kWh, as shown in Fig. 10(d). As a consequence, the generators in MG_A now share the total load in an optimal manner. During this condition, the SoC was 85 %, making the ESS cheaper. Therefore, the ESS picks larger share of load among the generators, while both the DGs reduce their share, as shown in the Fig. 10(b).

The same scenario was observed in MG_B at $t = t_2$, when its ER was enabled. The ESS being cheaper, ramps up its output while other DGs reduce their generation as their incremental costs become equal at steady state, as shown in Fig. 10(c) and (e). Further, the reduction in operating costs of both the MGs as the respective ERs were enabled is illustrated in Fig. 10(f). During both the events, it can be noted that the tie-line power was maintained at its reference value, as a result of which, the power distribution due to the action of ER in one MG does not affect the power distribution in the other MG. From both the cases presented, it can be validated that, despite various disturbances in the individual MGs, the tie-line controller was able to regulate the tie-line power at its scheduled value in a distributed manner.

C. Case-3: Case-1 and Case-2 Combined

In this case, the effect of simultaneous activation of tie-line controller and the ER is investigated. The simulation responses are shown in Fig. 11. At $t = t_1$, the tie-line controller and the

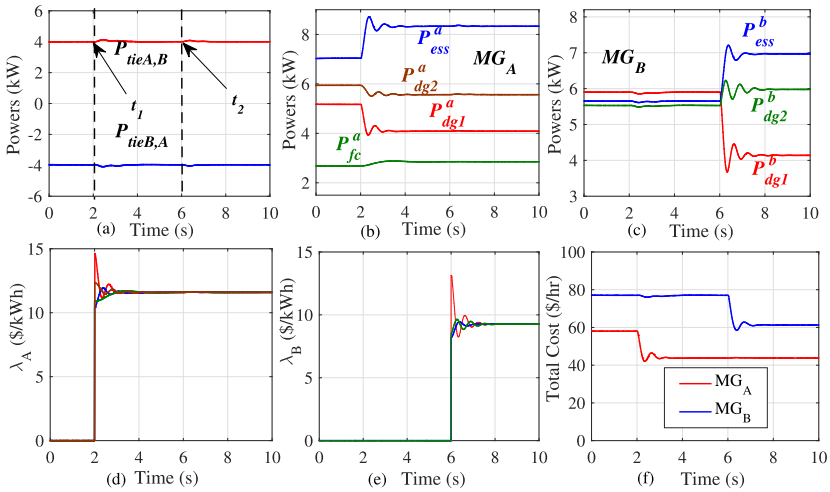

Fig. 10. Simulation results of case-2. (a) Tie-line power. (b) MG_A powers. (c) MG_B powers. (d) Incremental costs of MG_A. (e) Incremental costs of MG_B. (f) Total operating costs of MG_A and MG_B.

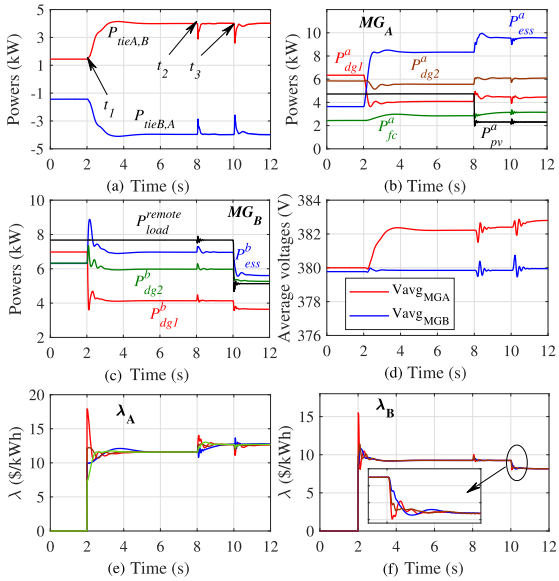

Fig. 11. Simulation results of case-3 combining case-1 and case-2. (a) Tie-line power. (b) MG_A powers. (c) MG_B powers. (d) Average voltages of both MGs. (e) Incremental costs of MG_A. (f) Incremental costs of MG_B.

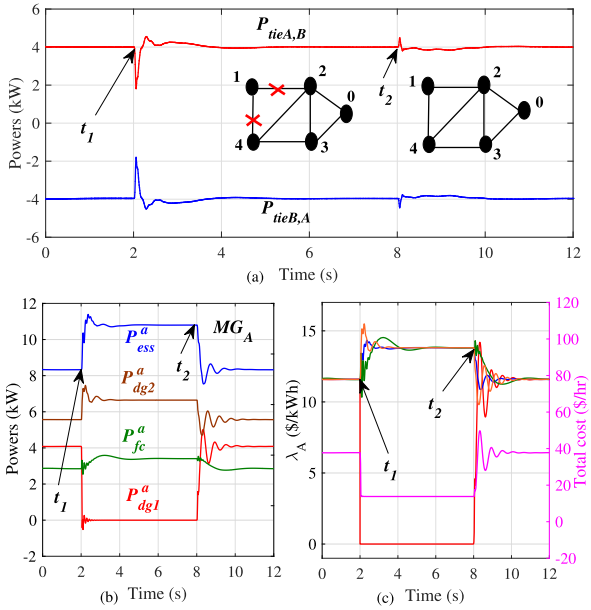

Fig. 12. Simulation results of case-4. (a) Tie-line power. (b) MG_A powers. (c) Incremental costs of MG_A (left y-axis), Total operating costs of MG_A (right y-axis).

ER both are activated simultaneously. While times t_2 and t_3 correspond to PV power change and load power change in MG_A and MG_B, respectively. Despite the various disturbances, the tie-line power was regulated at the reference value of 4 kW.

D. Case-4: Performance of Distributed Controllers Under Fault Conditions

This case highlights the MG operation under converter outage in MG_A. Initially, the tie-line power was maintained at 4 kW with ER and AVR in both MGs enabled. At $t = t_1$, due to some internal fault or forced outage, the DG_1 in MG_A gets isolated from the network. This is implemented by blocking the firing pulses to the DG converter, thereby forcing its output power to reduce to zero, as shown in Fig. 12(b). The corresponding communication links were also disabled, as shown in Fig. 12(a). The zero node shown in the cyber graph refers to the leader node (pinning node) connected to the nearby pinned nodes 2 and 3. Fig. 12(b) and (c) show the distribution of power, incremental costs and total operating cost in MG_A after t_1. It can be seen that post DG_1 outage, other generators quickly picked up the load. The transient power was picked by both the ESS and DG_2 while fuel-cell slowly ramps its output. At $t = t_2$, the pulses were de-blocked and the communications links were restored. It can be seen that the system regains its initial state as the generator power and its incremental cost settle to its previous value, as shown in Fig. 12(b) and (c), respectively. Even though the net generation remains same after the generator outage, the total generation cost (shown in pink color) in Fig. 12(c) reduces due

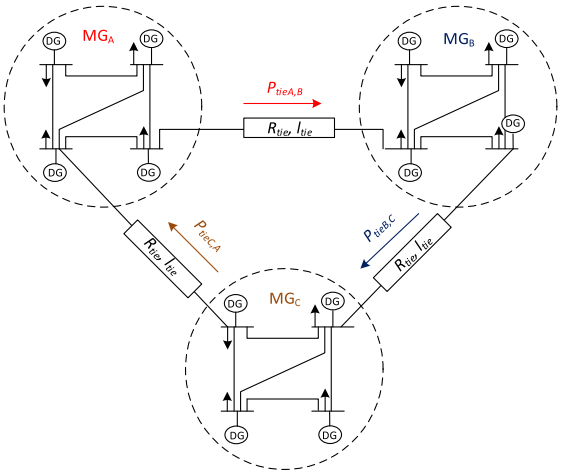

Fig. 13. Single line diagram representation of the studied three MG cluster where $P_{\text{tie}A,B}$ indicates positive power flow from MG_A to MG_B, $P_{\text{tie}B,C}$ indicates power flow from MG_B to MG_C, and $P_{\text{tie}C,A}$ indicates power flow from MG_C to MG_A.

to the outage of the relatively expensive generator (DG_1).This validates the performance of the proposed distributed control scheme, allowing the MG clusters to have plug and play operation as envisioned in a smart MG system.

VII. Extension to Multi-Microgrid Scenario

The schematic representation of the studied three MG system is shown in Fig. 13. Each MG cluster has four bus interconnected network. For brevity, only simulation responses of the tie-line power flows, PV/load powers, and MG average voltages are presented. The responses are presented in Fig. 16. In this case, initially all the controllers were enabled and tie-line powers $P_{\text{tie}A,B} = 5$ kW, $P_{\text{tie}B,C} = 2$ kW, and $P_{\text{tie}C,A} = -0.5$ kW were maintained. At $t = t_1$, the tie-line power reference of $P_{\text{tie}A,B}$ is changed from 5 to 3 kW. The tie-line power settles to the new value in about 3 s, as shown in Fig. 16(a). To further test the performance of the proposed control strategy, step increase in PV insolation in MG_A was made at $t = t_2$ causing its output power to increase from 7.6 to 15.2 kW. It can be seen that despite the disturbance, the tie-line power was effectively regulated at the reference. Similarly, at $t = t_3$, a step command of 4 kW was given to the MG_B tie-line controller. It can be seen that the corresponding tie-line power $P_{\text{tie}B,C}$ ramped up slowly and settled at the reference value in about 3 s. At $t = t_4$, a step reduction in remote load power in MG_B was made causing its output power to drop from 15.2 to 4.2 kW, as shown in Fig. 16(b). Again, $t = t_5$, the tie-line power reference of $P_{\text{tie}C,A}$ was increased from -0.5 to -2 kW. Lastly, at $t = t_6$, a step increase in remote load power in MG_C was introduced causing the load to increase from 7.8 to 13.66 kW. It can be seen that despite various disturbances, the tie-line powers was effectively regulated at their respective values.

The responses in Fig. 16(c) show the average MG voltages. At $t = t_1$, the average voltage of MG_A decreases (comes closer to the nominal value) since the tie-line power flow from MG_A to MG_B was reduced. In other words, the average voltage difference between MG_A and MG_B reduces as a consequence. At $t = t_3$, in order to increase the power flow from MG_B to MG_C, the controller raises the average voltage of MG_B with respect to MG_C. Similar explanation can be given for the event at $t = t_5$. For a large load reduction at $t = t_4$, it can be seen that the average MG voltages increase above the nominal. This change is attributed to the response of tie-line controller as it adjusts the MG average voltages so as to maintain the tie-line powers at the respective levels.

VIII. Real Time Simulation Results

This section presents the real-time simulation results demonstrating the tie-line control between two dc MG clusters. The central idea is to demonstrate the implementation of proposed distributed tie-line control strategy using an actual communication system. Every agent (local controller at a DG bus) receives information from its neighboring agents and transmits local set of information to the neighboring agents. In this experiment, the dc MG clusters are modeled and simulated in real-time in two separate cores (CPUs) inside OPAL-RT OP5600. The tie-line is modeled using the distributed power line model from the Artemis library of RT-LAB [31].

The schematic representation of the proposed approach is shown in Fig. 15. The control strategy, shown in Fig. 5, is implemented for the local control agents inside OPAL-RT simulator while the communication layer and the cyber graph is implemented using separate MATLAB scripts running in two different host computers. Ethernet communication using TCP/IP protocol is employed to transfer set of information from one local control agent to its neighboring agents according to the designed cyber graph, as shown in Fig. 15. Different ports are created for each control agent inside MG over which the information is exchanged. For example, port 7201 represents a dedicated channel for control agent at bus 1. The local controller transmits the consensus outputs such as its estimated average voltage ($\tilde{V}_{\text{av},1}$), tie-line consensus state (ΔV_1), and ER state (λ_1). Similarly, over the same port, it receives information from its neighboring agents 2 and 4 according to the designed cyber-graph. The rate of transmission in OPAL-RT is carefully designed for optimum controller performance and accordingly it was set at 1 Hz, which represents data transmission and reception every 1 s.

For brevity, only the responses of MG_A are presented, as shown in Fig. 14. In this test, three events were introduced at different instants namely t_1, t_2, and t_3. At $t = t_1$, the AVR was enabled; at $t = t_2$, ER was enabled; and lastly at $t = t_3$, the tie-line controller was enabled. Before $t = t_1$, the tie-line power flow was at -1.8 kW indicating power flow from MG_B to MG_B, as shown in Fig. 14(a). The average voltage of MG_A was found to be at 379.6 V, as shown in Fig. 14(f) where deviation of the average voltage from its nominal value of 380 is shown. After the AVR was enabled at t_1, it can be seen that the $\Delta V\text{avg}_{\text{MG}_A}$, shown in Fig. 14(f), goes to zero indicating that the average voltage becomes equal to the nominal value. Consequently, the tie-line power flow became zero since voltage differences at the boundary buses becomes nearly zero. At t_2, the ER was enabled

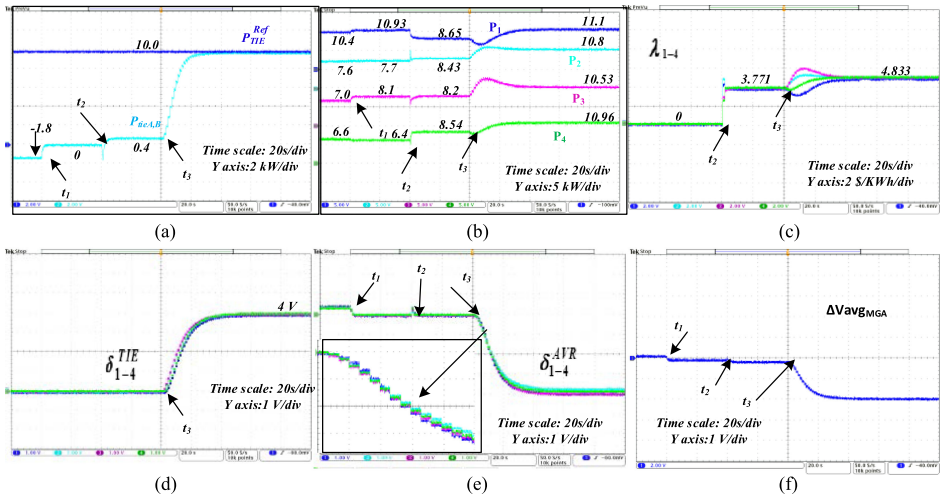

Fig. 14. Real-time simulation results with the distributed communication implemented using Ethernet-based TCP/IP communication. (a) Tie-line power. (b) MG_A powers. (c) Incremental costs of MG_A. (d) Consensus variables of the tie-line controller. (e) Consensus variables of the AVR. (f) MG_A average voltage deviation.

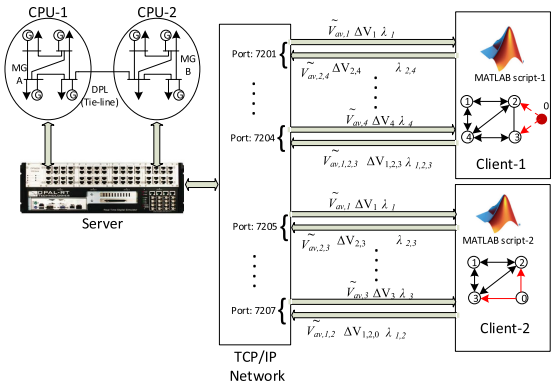

Fig. 15. Real-time simulation of the dc MG cluster using OPAL-RT real-time simulator with TCP/IP communication. The dc MGs, MG_A and MG_B are modeled in OPAL-RT while the communication cyber-graph is implemented using MATLAB scripts in two different host computers.

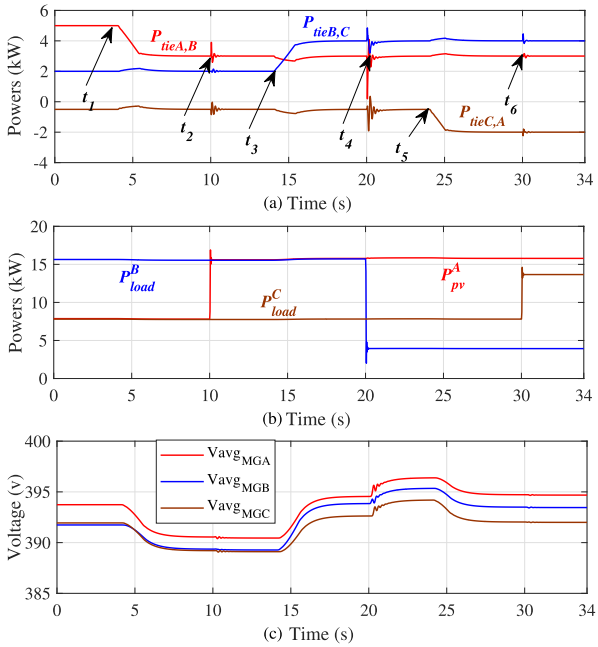

Fig. 16. Simulation results showing responses of three MG cluster. (a) Tie-line power. (b) PV power of MG_A, remote load power in MG_B and remote load power in MG_C. (c) Average voltages of three MGs.

following which the incremental costs, shown in Fig. 14(c), undergo consensus and settle at a value of 3.771 $/kWh. It can be seen that after t_2 the average voltage of the MG was still maintained close to the nominal value despite changes in power flow through the system caused by the operation of ER. Lastly, at t_3 the tie-line controller was enabled with the tie-line power reference set to 10 kW. A smooth tracking of tie-line power can be observed from Fig. 14(a) as the tie-line power flow reaches the reference of 10 kW. The tie-line controller increases the MG_A nominal voltage such that the requisite tie-line power flow is maintained. This validates the effectiveness of the proposed distributed tie-line control strategy implemented using Ethernet communication with TCP/IP protocol.

IX. Experimental Validation

An experimental setup of two dc MG clusters, as shown in Fig. 17, was prototyped, consisting of three controllable sources in each MG of 4 buses. The controllable sources are implemented using boost dc–dc converters where the input voltage is an unregulated dc supply obtained through uncontrolled single phase rectifiers. The input voltage to the boost converters was kept around 60 V and their output was regulated at 110 V. A network of five transmission lines similar to study system, shown in Fig. 1, interconnects the four buses in each MG. A constant power load is connected at bus 4 of MG_A. The constant power load is implemented using a buck dc–dc converter with output voltage regulated at 48 V and input as the network voltage of 110 V. A Chroma 62100H programmable dc power supply based PV emulator was used as a PV source with 0.6 kW rating and connected at bus 4 of MG_B. The proposed distributed

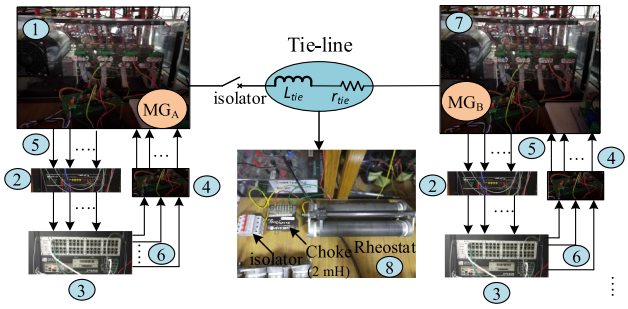

Fig. 17. Experimental setup of a four-bus dc MGs interconnected by a tie-line. (1) and (7) Four-leg isolated IGBT-based dc–dc converters representing four buses in MG_A and MG_B. (2) OP8662 sensor board. (3) OP5600 real-time Simulator. (4) Optocoupler circuit. (5) Measurements. (6) PWM pulses. (8) Tie-line.

TABLE III
EXPERIMENTAL SETUP PARAMETERS

Element	Technical Parameter	Specifications
Primary Controllers	Outer voltage loop (K_p,K_i) Inner current loop (K_p,K_i) Droop gain, (R_d)	0.5, 10 0.01, 75 0.25
AVR	K_p^{avr}, K_i^{avr}, y_{ij}	0.4, 10, 10
ER(MG_A)	K_p^{er}, K_i^{er}, z_{ij}	2, 10, 1
ER(MG_B)	K_p^{er}, K_i^{er}, z_{ij}	0.5, 5, 1
Tie-Line Controler	K_p^{tie}, K_i^{tie}, x_{ij}	0.05, 0.05, 1
Network parameters of MG_A	r_{12}, L_{12}, r_{14}, L_{14}, r_{23}, L_{23}, r_{24}, L_{24}, r_{34}, L_{34}	0.2 Ω & 1.11 mH, 0.2 Ω & 1.22 mH, 0.1 Ω & 1.21 mH, 0.1 Ω & 0.93 mH, 0.2 Ω & 1.93 mH
Network parameters of MG_B	r_{12}, L_{12}, r_{14}, L_{14}, r_{23}, L_{23}, r_{24}, L_{24}, r_{34}, L_{34}	0.2 Ω & 0.977 mH, 0.2 Ω & 0.9 mH, 0.2 Ω & 0.95 mH, 0.1 Ω & 2.121 mH, 0.2 Ω & 0.95 mH
Cost Coefficients of MG_A	a_1, b_1, c_1 a_2, b_2, c_2 a_3, b_3, c_3	0.005, 0.008, 5 0.006, 0.006, 3 0.004, 0.007, 7
Cost Coefficients of MG_B	a_1, b_1, c_1 a_2, b_2, c_2 a_3, b_3, c_3	0.007, 0.008, 5 0.005, 0.006, 3 0.004, 0.007, 7

control scheme was developed in OPAL-RT OP5600-based real time digital simulator. Further details regarding the parameters of the experimental setup are given in Table III. Three case studies have been carried out to validate the performance of the distributed control scheme. The first case demonstrates the performance of tie-line controller under normal operation while the second case illustrates the performance of ER and its effect of tie-line control. In addition, in order to exactly replicate the behavior of communication links, the effect of delay in the tie-line communication channels is studied in the third case.

A. Controller Performance Under Normal Operation

In this case, the performance of the tie-line controller was evaluated for different power references. Two power reference commands of 2 W and 0.15 kW were introduced at time instants t_1 and t_2, respectively, as shown in Fig. 18(a). The AVR and ER were enabled in both MGs with tie-line controller disabled till the instant t_1. Before t_1, the average voltage of MG_A was

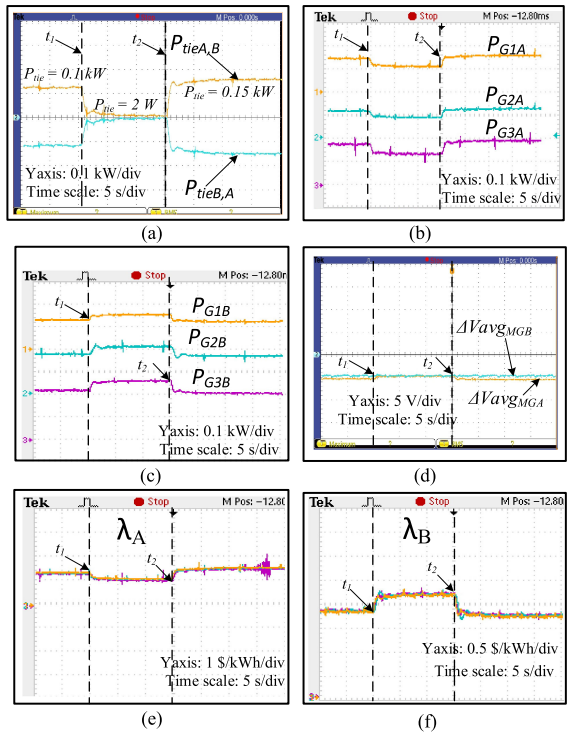

Fig. 18. Case-1: Experimental responses for step changes in tie-line references at $t = t_1$ and t_2. (a) Tie powers $P_{\text{tie}A,B}$ where suffix A,B corresponds to power flow from MG_A to MG_B. (b) and (c) MG_A powers and MG_B powers. (d) Voltage deviations of the average voltage from the nominal value. (e) and (f) Incremental costs of MG_A and MG_B, respectively.

controlled at 111 V with 110 V as the average voltage of MG_B. This causes a power flow of 0.11 kW from MG_A to MG_B. Total load in MG_A was approximately 0.55 kW and 0.74 kW in MG_B. P_{G1A}, P_{G2A}, and P_{G3A} are the power outputs of controllable sources in MG_A at buses 1, 2, and 3, respectively. Similarly, P_{G1B}, P_{G2B}, and P_{G3B} are the power outputs of controllable sources in MG_B at buses 1, 2, and 3, respectively. At $t = t_1$, the tie-line control was enabled in MG_A only, with a reference command equal to 2 W. The tie-line power reduces to 2 W and settles in 10 s, as shown in Fig. 18(a). As a result, the generation in MG_A reduces while it increases in MG_B to compensate for the reduction in tie-line import, as shown in Fig. 18(b) and (c), respectively. Fig. 18(d) shows the deviation of average voltage from a base value (arbitrary chosen) of 105 V. A negative ΔV of approximately 5 V exists due to the difference (105–110 V). It can be noticed that, the $\Delta V\text{avg}_{MG_A}$ tends to reduce after t_1 to reduce the tie power export $P_{\text{tie}A,B}$ to a low value of 2 W. After $t = t_2$, again a step command of 0.15 kW was given to the tie-line controller. The controller acts and increases the tie power to 0.15 kW in approximately 10 s. Finally, Fig. 18(e) and (f) show the responses of incremental costs of MG_A and MG_B, respectively.

B. Effect of ER on Tie-Line Control

This case is similar to the case-2 in the simulation results. The tie-line controller and AVR remain enabled throughout while the ER of both MGs were enabled at instants t_1 and t_2,

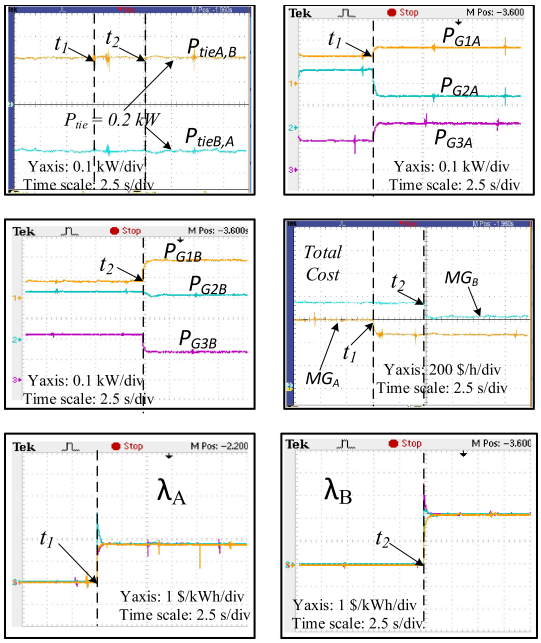

Fig. 19. Case-2: Responses of the system when ER of MG_A is enabled at $t = t_1$ and ER of MG_B is enabled at $t = t_2$. (a) Tie powers $P_{\text{tie}A,B}$. (b) and (c) MG_A powers and MG_B powers. (d) Total costs. (e) and (f) Incremental costs of MG_A and MG_B, respectively.

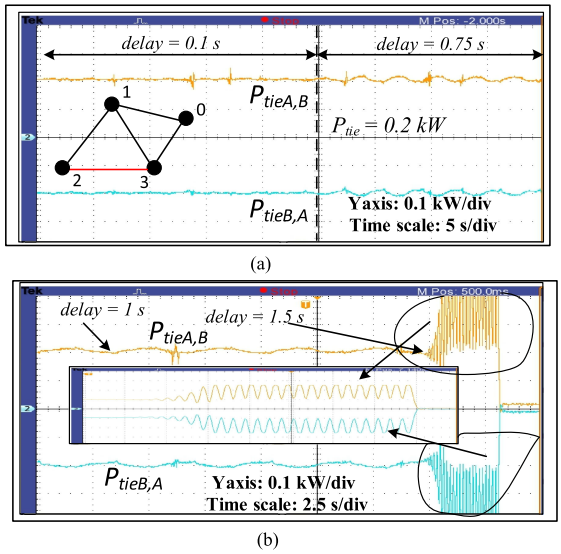

Fig. 20. Experimental responses of the tie-line power for different time delays in the communication channel 2–3 of the tie-line cyber graph. Red line indicates the affected communication channel due to delay.

respectively. Fig. 19 shows the various responses of the interconnected system. The tie-line power was regulated at 0.2 kW from MG_A to MG_B. Prior to t_1, the operating costs of MG_A and MG_B were equal to 600 $/hr and 720 $/hr, respectively, as shown in Fig. 19(d). After t_1, the operating cost of MG_A reduces to 460 $/hr due to the action of ER. Similarly, after t_2, the operating cost of MG_B reduces to 600 $/hr. Hence, this validates the role of ER in operating the system in an economical manner.

C. Effect of Delay on Tie-Line Control

The efficacy of distributed control strategy depends up on the reliability of networked communication system. Any practical communication system can be prone to various operational constraints such as limited bandwidth, congestion, jitters, latency, noise, fading, and the management of signal transmission power [32]. Particularly, the effect of latency can have a serious impact on the stability of networked control system such as distributed MG operation. Therefore, this case shows the effect of increasing delay in the communication channel 2–3 on the stability of the system. In this case the tie-line power was controlled at 0.2 kW with AVR and ER active in both the MGs. It can be seen from Fig. 20(a), that undamped oscillations began to appear in the tie-line power when delay in the channel connecting nodes 2 and 3 increased from 0.1 to 0.75 s. Further increase in the delay in channel from 1 to 1.5 s, aggravated the amplitude of oscillations, as shown in Fig. 20(b). The frequency of oscillation was around 8 Hz and the critical delay lies between 1 and 1.5 s.

X. Conclusion

This article has presented a distributed control strategy for tie-line power flow control between two interconnected and independently owned autonomous dc MG clusters. The considered architecture of dc MGs are of multibus type incorporating heterogeneous mix of energy sources such as DG, fuel-cell (FC), PV and BESS. Hierarchical control strategy based on distributed communication is adopted for both the MGs taking into account the modes of operation of these sources. The proposed control strategy will enable the respective MG owner to minimize the operating costs of the DG while taking into account the current SoC of BESS. Further, the tie-line controller unified with the average voltage regulation and ER is implemented in a distributed fashion using pinning consensus protocol which improves the reliability and lowers the cost of implementation compared to the centralized method. The small signal stability analysis of the studied system incorporated with distributed hierarchical control reveals the presence of low frequency but relatively stable modes. These modes are originated due to slow secondary and tertiary controllers as well as due to the gains in distributed consensus protocols which therefore demands a careful tuning of various parameters to achieve a desired speed of response along with enough stability margin in the system. Simulation results performed on two MG system under normal and faulty system conditions demonstrates the effectiveness and reliability of the proposed control philosophy. Simulations performed on a three MG three tie-line system proves the expandability of the proposed unified hierarchical control. The real-time simulation results demonstrate that the proposed distributed control philosophy is implementable using a real communication platform such as Ethernet-based TCP/IP communication. Lastly, experimental results demonstrate the practical implementation of the proposed distributed tie-line control strategy on a scaled laboratory setup.

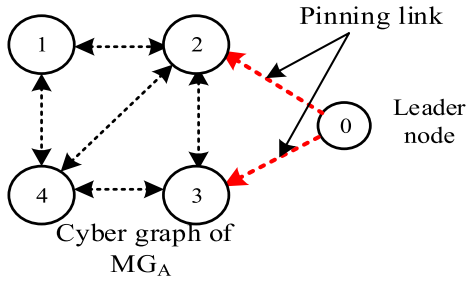

Fig. 21. Tie-line cyber graph of MG_A.

APPENDIX
SMALL SIGNAL MODELING OF THE DC MICROGRID CONSIDERING THE COMMUNICATION DELAY

In continuation to the modeling presented in subsection four of the Section IV, this section presents the modeling approach used in the DEs for an ith converter in addition to the DE model of the transcendental delay term.

The dynamic model governing the consensus of tie-line controller can be presented as

$$[\Delta\dot{\theta}] = -[L][\Delta\theta] \tag{59}$$

where $\Delta\theta$ represents the column vector corresponding to the states of the tie-line consensus and L is the Laplacian matrix corresponding to the cyber graph shown in Fig. 21. Equation (1) can be further expanded as

$$\begin{bmatrix}\Delta\dot{\theta}_0\\ \Delta\dot{\theta}_1\\ \Delta\dot{\theta}_2\\ \Delta\dot{\theta}_3\\ \Delta\dot{\theta}_4\end{bmatrix} = -\begin{bmatrix}2 & 0 & -1 & -1 & 0\\ 0 & 2 & -1 & -1 & 0\\ -1 & -1 & 4 & -1 & -1\\ -1 & 0 & -1 & 3 & -1\\ 0 & -1 & -1 & -1 & 3\end{bmatrix}\begin{bmatrix}\Delta\theta_0\\ \Delta\theta_1\\ \Delta\theta_2\\ \Delta\theta_3\\ \Delta\theta_4\end{bmatrix}. \tag{60}$$

Assuming channel 2–3 is experiencing a communication delay, then (2) can be modified as

$$\begin{bmatrix}\Delta\dot{\theta}_0\\ \Delta\dot{\theta}_1\\ \Delta\dot{\theta}_2^d\\ \Delta\dot{\theta}_3^d\\ \Delta\dot{\theta}_4\end{bmatrix} = -\begin{bmatrix}2 & 0 & -1 & -1 & 0\\ 0 & 2 & -1 & -1 & 0\\ -1 & -1 & 4 & -1 & -1\\ -1 & 0 & -1 & 3 & -1\\ 0 & -1 & -1 & -1 & 3\end{bmatrix}\begin{bmatrix}\Delta\theta_0\\ \Delta\theta_1\\ \Delta\theta_2^d\\ \Delta\theta_3^d\\ \Delta\theta_4\end{bmatrix} \tag{61}$$

where $\Delta\theta_2^d$ and $\Delta\theta_3^d$ are the states affected by the communication delay introduced in the channel 2–3. For modeling aspects, the transcendental term $e^{-s\tau_d}$ is employed to capture the communication delay in the communication network. Approximating the time delay using Pade approximation up to the first order we can write

$$e^{-s\tau_d} \approx \frac{1 - s\tau_d}{1 + s\tau_d}. \tag{62}$$

To incorporate the delay block to the small signal model of the system, the first order time delay block, shown in Fig. 22(a), can

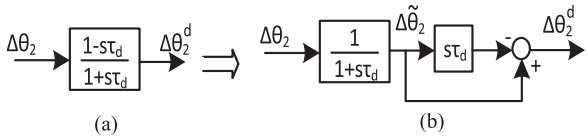

Fig. 22. (a) First order approximation of the time delay using Pade approximation. (b) Equivalent representation of the delay transfer function shown in (a).

be represented as a cascaded combination of blocks shown in Fig. 22(b). The advantage of this approach is that it allows to avoid the derivative part appearing in the numerator [33]. The DE governing the state of the first block can be written as

$$\frac{d\Delta\tilde{\theta}_2}{dt} = (1/\tau_d)(\Delta\theta_2 - \Delta\tilde{\theta}_2). \tag{63}$$

The output $(\Delta\theta_2^d)$ can be written in terms of the state variable $(\Delta\tilde{\theta}_2)$ as

$$\Delta\theta_2^d = \Delta\tilde{\theta}_2 - \tau_d\frac{d\Delta\tilde{\theta}_2}{dt} \tag{64}$$

$$= 2 * \Delta\tilde{\theta}_2 - \Delta\theta_2. \tag{65}$$

Similar approach is carried out for the state variable $\Delta\tilde{\theta}_3$. The voltage shift caused by the tie-line dynamics can be represented in matrix form as

$$[\Delta V] = \beta[\Delta\theta] \tag{66}$$

where β is the participation factor for the respective DG. The resultant ΔV from the tie-line dynamics is added with the nominal voltage to generate new reference for the AVR loop. In matrix form it can be written as

$$[\delta^{\mathrm{avr}}] = [G^{\mathrm{avr}}]\left\{\left[[V_o^{\mathrm{nom}}] + [\Delta V]\right] - [G_{\mathrm{est}}][V_o]\right\} \tag{67}$$

where δ^{avr} is the vector of state variables corresponding to AVR, $[G^{\mathrm{avr}}]$ is the square matrix with diagonal terms corresponding to the AVR PI controller, G_{est} is the square matrix whose diagonal elements contain the transfer function of voltage estimator, and V_o represents the vector of output voltages of the converter.

Finally, the delay model is augmented with rest of the system model to build the overall system closed loop state matrix, from which the eigenvalues are evaluated.

REFERENCES

[1] T. Dragicevic, X. Lu, J. C. Vasquez, and J. M. Guerrero, "DC microgrids-Part II: A review of power architectures, applications, and standardization issues," *IEEE Trans. Power Electron.*, vol. 31, no. 5, pp. 3528–3549, May 2016.

[2] T. Dragicevic, X. Lu, J. C. Vasquez, and J. M. Guerrero, "DC microgrids-Part I: A review of control strategies and stabilization techniques," *IEEE Trans. Power Electron.*, vol. 31, no. 7, pp. 4876–4891, Jul. 2016.

[3] P. Nuutinen *et al.*, "Research site for low-voltage direct current distribution in a utility network-structure, functions, and operation," *IEEE Trans. Smart Grid*, vol. 5, no. 5, pp. 2574–2582, Sep. 2014.

[4] K. Shenai, A. Jhunjhunwala, and P. Kaur, "Electrifying India: Using solar DC microgrids," *IEEE Power Electron. Mag.*, vol. 3, no. 4, pp. 42–48, Dec. 2016.

[5] Q. Shafiee, T. Dragicevic, J. C. Vasquez, and J. M. Guerrero, "Hierarchical control for multiple dc-microgrids clusters," *IEEE Trans. Energy Convers.*, vol. 29, no. 4, pp. 922–933, Dec. 2014.
[6] S. Sahoo and S. Mishra, "A multi-objective adaptive control framework in autonomous dc microgrid," *IEEE Trans. Smart Grid*, vol. 9, no. 5, pp. 4918–4929, Sep. 2018.
[7] S. Sahoo and S. Mishra, "An adaptive event-triggered communication-based distributed secondary control for dc microgrids," *IEEE Trans. Smart Grid*, vol. 9, no. 6, pp. 6674–6683, Nov. 2018.
[8] S. Anand, B. G. Fernandes, and J. Guerrero, "Distributed control to ensure proportional load sharing and improve voltage regulation in low-voltage dc microgrids," *IEEE Trans. Power Electron.*, vol. 28, no. 4, pp. 1900–1913, Apr. 2013.
[9] V. Nasirian, A. Davoudi, F. L. Lewis, and J. M. Guerrero, "Distributed adaptive droop control for dc distribution systems," *IEEE Trans. Energy Convers.*, vol. 29, no. 4, pp. 944–956, Dec. 2014.
[10] S. Moayedi and A. Davoudi, "Unifying distributed dynamic optimization and control of islanded dc microgrids," *IEEE Trans. Power Electron.*, vol. 32, no. 3, pp. 2329–2346, Mar. 2017.
[11] V. Nasirian, S. Moayedi, A. Davoudi, and F. L. Lewis, "Distributed cooperative control of dc microgrids," *IEEE Trans. Power Electron.*, vol. 30, no. 4, pp. 2288–2303, Apr. 2015.
[12] L. Che and M. Shahidehpour, "DC microgrids: Economic operation and enhancement of resilience by hierarchical control," *IEEE Trans. Smart Grid*, vol. 5, no. 5, pp. 2517–2526, Sep. 2014.
[13] H. Wang, M. Han, J. M. Guerrero, J. C. Vasquez, and B. G. Teshager, "Distributed secondary and tertiary controls for I–V droop-controlled-paralleled dc–dc converters," *IET Gener., Transm. Distrib.*, vol. 12, no. 7, pp. 1538–1546, 2018.
[14] L. Che, M. Shahidehpour, A. Alabdulwahab, and Y. Al-Turki, "Hierarchical coordination of a community microgrid with ac and dc microgrids," *IEEE Trans. Smart Grid*, vol. 6, no. 6, pp. 3042–3051, Nov. 2015.
[15] L. Meng *et al.*, "Review on control of dc microgrids and multiple microgrid clusters," *IEEE J. Emer. Sel. Topics Power Electron.*, vol. 5, no. 3, pp. 928–948, Sep. 2017.
[16] D. H. Tungadio, R. C. Bansal, and M. W. Siti, "Optimal control of active power of two micro-grids interconnected with two ac tie-lines," *Electric Power Compon. Syst.*, vol. 45, no. 19, pp. 2188–2199, 2017. [Online]. Available: https://doi.org/10.1080/15325008.2017.1384940
[17] Y. Li, N. Liu, and J. Zhang, "Jointly optimization and distributed control for interconnected operation of autonomous microgrids," in *Proc. IEEE Innovative Smart Grid Technol. - Asia*, Nov. 2015, pp. 1–6.
[18] M. Nasir, Z. Jin, H. A. Khan, N. A. Zaffar, J. C. Vasquez, and J. M. Guerrero, "A decentralized control architecture applied to dc nanogrid clusters for rural electrification in developing regions," *IEEE Trans. Power Electron.*, vol. 34, no. 2, pp. 1773–1785, Feb. 2019.
[19] T. Dragievi, J. M. Guerrero, and J. C. Vasquez, "A distributed control strategy for coordination of an autonomous LVDC microgrid based on power-line signaling," *IEEE Trans. Ind. Electron.*, vol. 61, no. 7, pp. 3313–3326, Jul. 2014.
[20] X. Li *et al.*, "Flexible interlinking and coordinated power control of multiple dc microgrids clusters," *IEEE Trans. Sustain. Energy*, vol. 9, no. 2, pp. 904–915, Apr. 2018.
[21] Y. Xia, W. Wei, M. Yu, X. Wang, and Y. Peng, "Power management for a hybrid ac/dc microgrid with multiple subgrids," *IEEE Trans. Power Electron.*, vol. 33, no. 4, pp. 3520–3533, Apr. 2018.
[22] S. Moayedi and A. Davoudi, "Distributed tertiary control of dc microgrid clusters," *IEEE Trans. Power Electron.*, vol. 31, no. 2, pp. 1717–1733, Feb. 2016.
[23] J. Hu, Y. Li, T. Yong, J. Cao, J. Yu, and W. Mao, "Distributed cooperative regulation for multiagent systems and its applications to power systems: A survey," *Sci. World J.*, vol. 2014, 2014, Art. no. 139028.
[24] J. Xiao, P. Wang, and L. Setyawan, "Implementation of multiple-slack-terminal dc microgrids for smooth transitions between grid-tied and islanded states," *IEEE Trans. Smart Grid*, vol. 7, no. 1, pp. 273–281, Jan. 2016.
[25] M. E. Susetyo, N. Hariyanto, A. Rizqiawan, and S. A. Sitompul, "Droop control implementation on hybrid microgrid PV-diesel-battery," in *Proc. Int. Conf. High Voltage Eng. Power Syst.*, Oct. 2017, pp. 295–300.
[26] R. K. Sharma and S. Mishra, "Dynamic power management and control of a PV PEM fuel-cell-based standalone ac/dc microgrid using hybrid energy storage," *IEEE Trans. Ind. Appl.*, vol. 54, no. 1, pp. 526–538, Jan. 2018.
[27] L. Meng *et al.*, "Distributed voltage unbalance compensation in islanded microgrids by using a dynamic consensus algorithm," *IEEE Trans. Power Electron.*, vol. 31, no. 1, pp. 827–838, Jan. 2016.
[28] S. Yang, S. Tan, and J. Xu, "Consensus based approach for economic dispatch problem in a smart grid," *IEEE Trans. Power Syst.*, vol. 28, no. 4, pp. 4416–4426, Nov. 2013.
[29] R. de Azevedo, M. H. Cintuglu, T. Ma, and O. A. Mohammed, "Multiagent-based optimal microgrid control using fully distributed diffusion strategy," *IEEE Trans. Smart Grid*, vol. 8, no. 4, pp. 1997–2008, Jul. 2017.
[30] F. Chen, Z. Chen, L. Xiang, Z. Liu, and Z. Yuan, "Reaching a consensus via pinning control," *Automatica*, vol. 45, no. 5, pp. 1215–1220, 2009.
[31] C. Dufour, J. Mahseredjian, and J. Belanger, "A combined state-space nodal method for the simulation of power system transients," *IEEE Trans. Power Del.*, vol. 26, no. 2, pp. 928–935, Apr. 2011.
[32] J. Baillieul and P. J. Antsaklis, "Control and communication challenges in networked real-time systems," *Proc. IEEE*, vol. 95, no. 1, pp. 9–28, Jan. 2007.
[33] P. Kundur, N. J. Balu, and M. G. Lauby, *Power System Stability and Control*. New York, NY, USA: McGraw-Hill, 2009.

Shivraman Mudaliyar (Student Member, IEEE) received the B.E. degree in electrical engineering from Anna University, Chennai, India, in 2005, and the M.Tech. degree in power and energy systems engineering from the National Institute of Technology Silchar, Assam, India, in 2015. He is currently working towards the Ph.D. degree in electrical engineering with the Indian Institute of Technology Delhi, Delhi, India.

He has work experience of both academia as well as industry. He was a Junior Engineer-1 (Operation & Maintenance) with Jodhpur DISCOM, Jodhpur, India. His research interests include power flow control in dc microgrids, optimal control, and power management of distributed generation in ac–dc microgrid.

Bhanu Duggal received the B.E. degree in electrical engineering from Thapar University, Patiala, India, in 2017, and the M.Sc. degree in future power networks from Imperial College London, London, U.K., in 2019.

He is currently an Associate Member with the Energy Institute (EI), London. His research interests include energy management of distributed energy resources, smart grids, and emerging power markets.

Sukumar Mishra (Senior Member, IEEE) received the M.Sc. and Ph.D. degrees in electrical engineering from Regional Engineering College Rourkela, Rourkela, India, in 1992 and 2000, respectively.

He is currently a Professor with the Indian Institute of Technology (IIT) Delhi, New Delhi, India, and has been a part of the IIT Delhi for the past 15 years. He authored or coauthored more than 200 research articles (including papers in international journals, conferences, and book chapters). His research interests include power systems, power quality studies, renewable energy, and smart grids.

Prof. Mishra is currently an Editor for the IEEE TRANSACTIONS ON SMART GRID and an Associate Editor for the *IET Generation, Transmission & Distribution*. He is the Vice-Chair of the Intelligent System Subcommittee of IEEE Power and Energy Society. Apart from all research and academic collaborations, he is very actively involved in industrial collaborations. He is currently the acting INAE Chair Professor and has been previously delegated as the NTPC and Power Grid Chair Professor. He is also the Independent Director of the Cross Border Power Transmission Company Ltd. and the River Engineering Pvt. Ltd. He has won many accolades throughout his academic tenure of 25 years. He was the recipient of the INSA Medal for Young Scientist in 2002, the INAE Young Engineer Award in 2009, the INAE Silver Jubilee Young Engineer Award in 2012, and the Samanta Chandra Shekhar Award in 2016. He has been granted fellowship from many prestigious technical societies, such as IET (U.K.), NASI (India), INAE (India), IETE (India), and IE (India), and is also recognized as the INAE Industry Academic Distinguish Professor.